

From Bell products to Greenberger-Horne-Zeilinger states: Quantum memories via emergent Hamiltonians

Anubhab Sur ^{1,2,*}, Qiujiang Guo ^{3,†} and Rubem Mondaini ^{1,2,‡}

¹*Department of Physics, University of Houston, Houston, Texas 77004, USA*

²*Texas Center for Superconductivity, University of Houston, Houston, Texas 77004, USA*

³*School of Physics, ZJU-Hangzhou Global Scientific and Technological Innovation Center, and Zhejiang Key Laboratory of Micro-nano Quantum Chips and Quantum Control, Zhejiang University, Hangzhou 310058, China*

With the advent of exquisite quantum emulators, storing highly entangled many-body states becomes essential. While entanglement typically builds over time when evolving a quantum system initialized in a product state, freezing that information at any given instant requires quenching to a Hamiltonian with the time-evolved state as an eigenstate, a concept we realize via an emergent Hamiltonian framework. While the emergent Hamiltonian is generically nonlocal and may lack a closed form, we show examples where it is exact and local, thereby enabling, in principle, indefinite state storage limited only by experimental imperfections. Unlike other phenomena, such as many-body localization, our method preserves both local and global properties of the quantum state. In some of our examples, we demonstrate that this protocol can be used to store maximally entangled multiqubit states, such as tensor products of Bell states, or fragile, globally distributed entangled states, in the form of Greenberger-Horne-Zeilinger states, which are often challenging to initialize in actual devices.

I. INTRODUCTION

Storing highly entangled quantum states without degradation is an essential challenge for applications in quantum computing and quantum emulation. In this quest, the many-body localization (MBL) phenomenon [1–4], arising from the application of quenched disorder, has often been thought of as one of the best candidates for storing quantum states and thereby for quantum memory applications [5, 6]. Although MBL is relatively robust against small decoherence [7–9], one of its primary caveats is its inability to preserve most global properties of the state. In particular, the preserved memory achieved via MBL is primarily local, such as the preservation of few-body observables [10–16]. All nonlocal quantum correlations of the system tend to vary with time, and most of the nonlocal memory of the system fades. Indeed, the total entanglement of the system also grows, albeit slowly [17–19], signaling nontrivial dynamics and gradual change of the state over time [20].

A fundamentally different and robust approach is provided by quantum error correction (QEC), which can be set as active [21], wherein quantum information is distributed among many qubits and periodically recovered as needed via an error-reversal procedure [22] or passive, in which the entangled state one aims to store is the ground state of a stabilizer Hamiltonian [23]. Unlike MBL, QEC can preserve both local and nonlocal correlations. Nonetheless, large-scale experimental implementation of either passive or active schemes remains challenging [24, 25].

Alternatively, in the noisy intermediate-scale quantum (NISQ) era of quantum computation, involving hundreds of imperfect qubits, another major challenge arises from the need to rapidly switch back and forth from idle qubits when not in operation to a strongly interacting regime during multiqubit operations [26]. For instance, a designed multiqubit gate can couple qubits, generating a highly entangled state. Switching off such a gate, effectively promoting an identity operation, can be interpreted as a quantum memory. Yet, this quick switch between strong mutual coupling and idling (“doing nothing”) must be done efficiently in a way that there are minimal leaks during the idling phase—current platforms have an estimated error via information leakage in this regime of up to 10% [27].

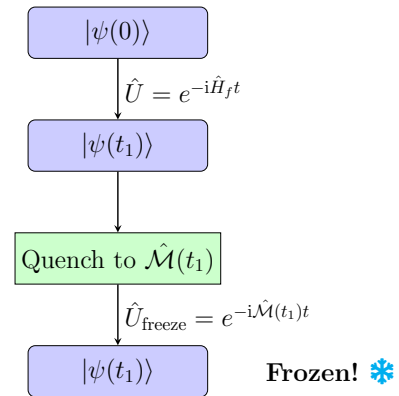


FIG. 1. Schematics of the protocol. We freeze the dynamics at time $t = t_1$ via carrying out a quench from the entangling Hamiltonian \hat{H}_f to $\hat{M}(t_1)$ —the emergent or freezing Hamiltonian defined at t_1 .

* asur3@uh.edu

† qguo@zju.edu.cn

‡ rmondaini@uh.edu

Thus, we seek an alternative approach that can pro-

vide stronger and more reliable protection for quantum states, preserving both local and nonlocal correlations more effectively. A mechanism to accomplish that can be obtained by a protocol dubbed "emergent Hamiltonian" [28, 29], wherein after promoting a unitary dynamics generated by an arbitrary Hamiltonian \hat{H}_f of some generic, often unentangled, initial state, the time-evolved state becomes an eigenstate of an operator $\hat{\mathcal{M}}(t)$. This operator assumes the form

$$\hat{\mathcal{M}}(t) = e^{-i\hat{H}_f t} \hat{H}_0 e^{i\hat{H}_f t} = \hat{H}_0 + \sum_{n=1}^{\infty} \frac{(-it)^n}{n!} \hat{\mathcal{H}}_n, \quad (1)$$

where $\hat{\mathcal{H}}_n \equiv [\hat{H}_f, [\hat{H}_f, \dots, [\hat{H}_f, \hat{H}_0] \dots]]$ is a nested n th order commutator, and the operator \hat{H}_0 is chosen such that the initial state is one of its eigenstates. It is easy to see that $|\psi(t)\rangle$ is an eigenstate of $\hat{\mathcal{M}}$: $e^{-i\hat{H}_f t} \hat{H}_0 e^{i\hat{H}_f t} |\psi(t)\rangle = e^{-i\hat{H}_f t} \hat{H}_0 |\psi(0)\rangle = E_0 e^{-i\hat{H}_f t} |\psi(0)\rangle = E_0 |\psi(t)\rangle$, where E_0 is the energy associated with the initial state in the Hamiltonian \hat{H}_0 . However, such a quantity generally leads to a highly nonlocal operator, precluding its identification as a physical Hamiltonian. Since the series expansion explicitly depends on the time t , the short-time dynamics are governed by the first few terms. Typically, the spatial support of the products of the operators involved is extended by each nonvanishing commutator in the series, resulting in the nested commutator being sufficiently local at $t \ll 1$ [28, 29], thus giving rise to an emergent physical Hamiltonian only in this regime.

Building on this, one of our motivations is to develop a protocol capable of pausing the dynamics of a quantum system indefinitely and with perfect precision without necessarily idling the qubits—Fig. 1 summarizes this. As previously suggested [28, 29], the key idea is that, at any moment during the evolution, the dynamics can be frozen by implementing a quench that transitions from the evolving Hamiltonian \hat{H}_f to the constructed emergent Hamiltonian $\hat{\mathcal{M}}(t)$ defined at the exact time t of the quench, resulting in complete freezing of the evolution, and thus preserving the entire quantum state at that time.

Although this protocol is universal and, in principle, applicable to freezing *any* unitary dynamics, it is particularly efficient and more meaningful in certain special scenarios, some of which we explore in this article. As mentioned above, the emergent Hamiltonian may be a highly nonlocal operator, which acts as a bottleneck in many cases. Our goal is to explore scenarios where we can derive a compact emergent Hamiltonian exactly at all times, thereby rendering this protocol perfect and exact, as well as others where obtaining a closed-form expression is challenging.

The presentation is divided as follows. In Sec. II, we introduce the emergent Hamiltonian in a one-dimensional (1D) system and investigate the dynamics of the entanglement entropy in many-body systems. Section III

generalizes the exact Emergent Hamiltonians for single-particle systems in higher dimensions, contrasting with an approximate case in the many-body regime. A spectral analysis is carried out in Sec. IV. We look at preparation and storage of Greenberger-Horne-Zeilinger (GHZ) states in Sec. V, and our findings are summarized in Sec. VI. Throughout this work we set $\hbar = 1$, and all times are therefore expressed in inverse energy units.

II. MODEL IN ONE DIMENSION

We start with a model Hamiltonian defined on a chain with open boundary conditions,

$$\hat{H}_f = \sum_l \left(J_l \hat{a}_{l+1}^\dagger \hat{a}_l + \text{H.c.} \right), \quad (2)$$

where \hat{a}_l^\dagger (\hat{a}_l) is the hard-core bosonic creation (annihilation) operator at site l . Unlike common bosons, these obey the hard-core constraint $(\hat{a}_l)^\dagger = (\hat{a}_l)^\dagger = 0$, preventing multiple occupancy at a single site [30]. Using the standard mapping between hard-core boson to spin-1/2 ladder operators $\hat{a}_l^\dagger = \hat{\sigma}_l^+$ ($\hat{a}_l = \hat{\sigma}_l^-$) [31] in Eq. (2), one can associate a lattice with L sites with that of an L -qubit system, where each site represents a qubit that is either excited (1) or not (0); the corresponding excitations can hop between consecutive qubits with amplitude J_l .

In particular, choosing the hopping amplitudes as $J_l = \frac{1}{2} \sqrt{l(L-l)}$ [32, 33] makes the hopping amplitude matrix $[J_{k,l}]$ resemble that of a large-spin matrix, rendering the Hamiltonian as

$$\begin{aligned} \hat{H}_f &= \sum_l \left(\frac{\sqrt{l(L-l)}}{2} \hat{\sigma}_{l+1}^+ \hat{\sigma}_l^- + \text{H.c.} \right) \\ &= \frac{\hat{S}_+ + \hat{S}_-}{2} = \hat{S}_x. \end{aligned} \quad (3)$$

Here, \hat{S}_\pm and \hat{S}_x are spin operators with spin quantum number $s = \frac{L-1}{2}$, and the second equality holds, in principle, when restricting to the single-excitation subspace. In this one-dimensional case, however, this mapping is still valid for any number of excitations due to the Jordan-Wigner transformation, $\hat{a}_l = e^{i\pi(\sum_{m<l} \hat{c}_m^\dagger \hat{c}_m)} \hat{c}_l$ with \hat{c}_l the fermionic annihilation operator, where the system can then be cast as a collection of noninteracting fermions, each of which is mapped by a large spin. That is, using the single-excitation matrix and imposing fermionic statistics via the Slater determinant on single-fermion dynamics, the system effectively describes multiple noninteracting large spins precessing with the same Hamiltonian $\hat{H}_f = \hat{S}_x = \sum_l \left(\frac{\sqrt{l(L-l)}}{2} \hat{c}_{l+1}^\dagger \hat{c}_l + \text{H.c.} \right)$. This is a key distinction from the higher-dimensional case discussed later, where the Jordan-Wigner transformation introduces nontrivial phase factors, preventing a straightforward reduction to a single-particle picture. In

two dimensions, therefore, we must rely on the hard-core bosonic description and consider the full many-body Hamiltonian.

Following the prescription in Ref. [28], we calculate the emergent Hamiltonian $\hat{\mathcal{M}}(t)$, taking the initial state as an eigenstate of a simple, diagonal in the computational basis, Hamiltonian \hat{H}_0 ,

$$\hat{H}_0 = \sum_{l=0}^{L-1} l \hat{a}_l^\dagger \hat{a}_l = \sum_{l=0}^{L-1} l \hat{c}_l^\dagger \hat{c}_l = -\hat{S}_z + \frac{L-1}{2} \hat{N}, \quad (4)$$

where we used the Jordan-Wigner transformation in the second equality, and $\hat{N} = \sum_l \hat{c}_l^\dagger \hat{c}_l$ is the total particle number operator. Unlike the case of homogeneous hoppings [29], in this case, the series that results in $\hat{\mathcal{M}}(t)$ [Eq. (1)] can be precisely summed by making the identifications of the nested commutators, $\hat{H}_{2n} = -\hat{S}_z$ and $\hat{H}_{2n+1} = i\hat{S}_y$, when using the standard spin commutation relations, $[\hat{S}_\alpha, \hat{S}_\beta] = i\epsilon_{\alpha\beta\gamma} \hat{S}_\gamma$, yielding

$$\begin{aligned} \hat{\mathcal{M}}(t) &= -\hat{S}_z + \frac{L-1}{2} \hat{N} \\ &+ \sum_{n=1,3,\dots}^{\infty} \frac{(-it)^n}{n!} i\hat{S}_y - \sum_{n=2,4,\dots}^{\infty} \frac{(-it)^n}{n!} \hat{S}_z \\ &= \frac{L-1}{2} \hat{N} + \sin(t) \hat{S}_y - \cos(t) \hat{S}_z. \end{aligned} \quad (5)$$

Thus, we provide an analytically exact expression of the emergent many-body Hamiltonian in a quadratic, local form—a sum of diagonal and nearest-neighbor “hopping” terms in Eq. (5), when casting in terms of hard-core bosonic operators:

$$\begin{aligned} \hat{\mathcal{M}}(t) &= \sum_{l=0}^{L-1} \left[\frac{L-1}{2} + \cos(t) \left(l - \frac{L-1}{2} \right) \right] \hat{a}_l^\dagger \hat{a}_l \\ &+ \sin(t) \sum_{l=1}^{L-1} \left(\frac{i\sqrt{l(L-l)}}{2} \hat{a}_l^\dagger \hat{a}_{l-1} + \text{H.c.} \right) \end{aligned} \quad (6)$$

A fundamental characteristic of the dynamics generated by \hat{H}_f is that it enables the preparation of highly entangled states from simple, easily initialized separable states such as product states. For example, Fig. 2 illustrates the time evolution of the half-chain entanglement entropy \mathcal{S}_A [$\mathcal{S}_A = -\sum_\alpha \lambda_\alpha^2 \log_2 \lambda_\alpha^2$, where λ_α are Schmidt coefficients] for two initial product states [34], a density wave, $|\psi(0)\rangle = |1010\dots 10\rangle$ [Fig. 2(a)] and a domain wall $|\psi(0)\rangle = |111\dots 000\rangle$ [Fig. 2(b)] — any product state is an eigenstate of \hat{H}_0 . Starting from these separable initial states, $\mathcal{S}_A(t=0) = 0$, the entanglement entropy and $|\psi(t)\rangle$ evolve periodically with a fundamental period of 2π , consistent with expectations from the spin mapping. At odd multiples of π , the roles of occupied and unoccupied sites are interchanged, yielding another separable state, i.e., $|\psi(t = (2n+1)\pi)\rangle = \prod_l \hat{\sigma}_x^{(l)} |\psi(t=0)\rangle$, where $n \in \mathbb{Z}_{\geq 0}$. This can be confirmed by the computation of the Hamming distance between these two

product states, $d_H(|n\rangle, |m\rangle) \equiv \sum_{l=0}^{L-1} |n_l - m_l|$ with $|n\rangle = |n_0 n_1 \dots n_{L-1}\rangle$ and $|m\rangle = |m_0 m_1 \dots m_{L-1}\rangle$, showing that $d_H(|\psi(t=0)\rangle, |\psi(t=\pi)\rangle) = L$ [Figs. 2(c) and 2(d)] — it relates to the perfect quantum state transfer protocol [33], now applied to a many-body state.

Notably, for the case of the density-wave initial state at times odd multiples of $\pi/2$, \mathcal{S}_A reaches its peak [Fig. 2(a)], corresponding to maximally entangled states with the highest possible Schmidt rank $r = 2^{L/2}$, with all Schmidt coefficients λ_α in the half-chain decomposition $|\psi(t)\rangle = \sum_{\alpha=0}^r \lambda_\alpha |n_A\rangle \otimes |n_B\rangle$ being equal [Fig. 2(e)] — a property never observed for domain wall initial states [Fig. 2(f)], explaining why the entanglement entropy is typically small for the latter. Thus, by quenching the dynamics at special times, $t_{\text{freeze}} = (2n+1)\pi/2$, from \hat{H}_f to $\hat{\mathcal{M}}(t_{\text{freeze}})$ in Eq. (5), one can efficiently prepare and store maximally entangled states when starting from a simple density-wave product state, as exemplified in Fig. 2(a).

In particular, the nature of these states can be compactly written (for an even L) as

$$\begin{aligned} |\psi(t = \pi/2)\rangle &= \bigotimes_{l=0}^{\frac{L}{2}-1} \frac{|1\rangle_l |0\rangle_{L-1-l} - i |0\rangle_l |1\rangle_{L-1-l}}{\sqrt{2}} \\ &= \bigotimes_{l=0}^{\frac{L}{2}-1} |\Psi\rangle_{l, L-1-l}, \end{aligned} \quad (7)$$

namely, a tensor product of pairwise entangled states $|\Psi\rangle \equiv \frac{|10\rangle - i|01\rangle}{\sqrt{2}}$ between inversion-symmetric qubits in the chain. A similar state with a different phase is obtained at time $t = 3\pi/2$.

From an experimental perspective, preparing such a nonlocal pairwise entangled state is straightforward only with all-to-all connectivity, where each pair can be generated in parallel through standard initialization of Bell-like states [35], requiring a circuit depth of four layers. The great majority of quantum circuits use a local (often nearest neighbor) connectivity [15, 36, 37], however. As such, creating such long-range entanglement necessarily entails a circuit depth that is extensive in the number of qubits. Our approach, on the other hand, even leveraging only nearest-neighbor connectivity, enables the creation of this state via unitary dynamics generated by \hat{H}_f and its subsequent storage by quenching to the corresponding emergent Hamiltonian $\hat{\mathcal{M}}(t)$ [Eq. (5)].

III. TWO DIMENSIONS

We now extend the entangling Hamiltonian \hat{H}_f to a two-dimensional (2D) lattice with $L_x \times L_y$ sites:

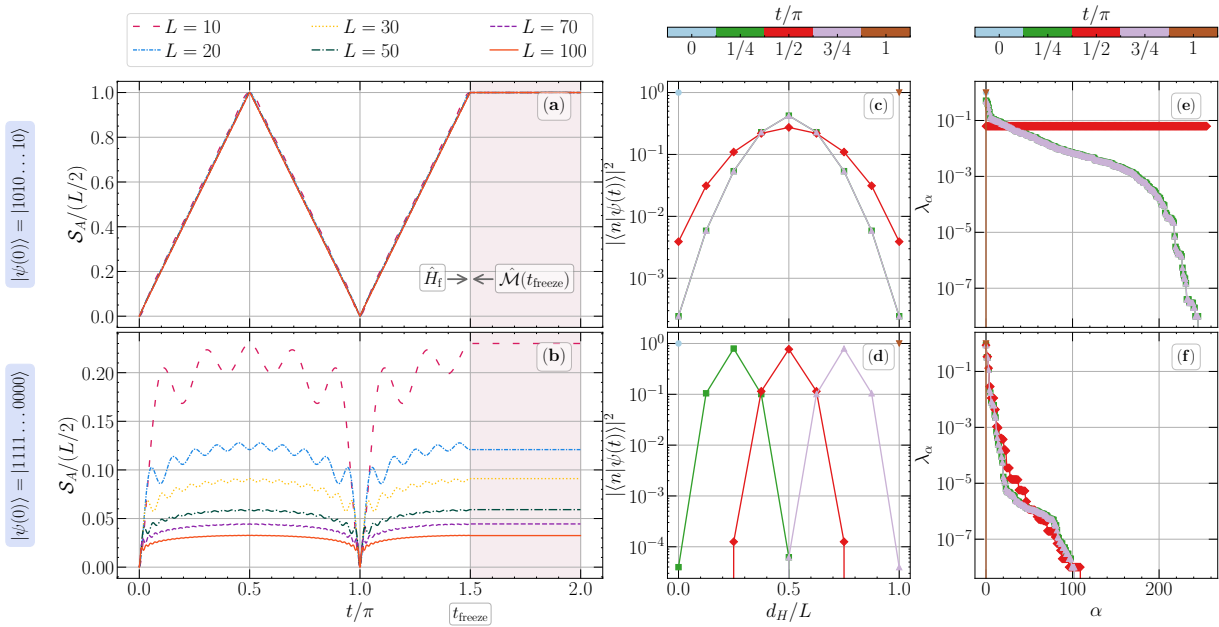


FIG. 2. Dynamics of the half-chain entanglement entropy, scaled by the maximal entropy, considering different chain sizes, for (a) density-wave [(b) domain wall] initial product state $|\psi(0)\rangle$; a quench $\hat{H}_f \rightarrow \hat{\mathcal{M}}$ is performed at $t_{\text{freeze}} = 3\pi/2$. (c) and (d) Distribution of Hamming distances and the corresponding weights $|\langle n|\psi(t)\rangle|^2$ in the time-dependent state $|\psi(t)\rangle$ of the Fock states $|n\rangle$, at representative times in the dynamics. (e) and (f) Schmidt coefficients of the half-chain decomposition at similar times. In (c) and (d), the system size is $L = 16$; as indicated, (a), (c), and (e) [(b), (d), and (f)] refer to the density-wave [domain wall] initial product state.

TABLE I. Comparison of approaches to extract the emergent Hamiltonian for single and many excitations in 1D and 2D systems.

	Single excitation	Many particles
1D	Exact closed form	Exact closed form
2D	Exact closed form	Approximate methods

$$\begin{aligned}
\hat{H}_f &= \sum_{\mathbf{l}} \frac{\sqrt{l_x(L_x - l_x)}}{2} \left(\hat{a}_{\mathbf{l}+\hat{x}}^\dagger \hat{a}_{\mathbf{l}} + \text{H.c.} \right) \\
&+ \sum_{\mathbf{l}} \frac{\sqrt{l_y(L_y - l_y)}}{2} \left(\hat{a}_{\mathbf{l}+\hat{y}}^\dagger \hat{a}_{\mathbf{l}} + \text{H.c.} \right) \quad (8) \\
&= \hat{S}_{1x} \otimes \hat{I}_2 + \hat{I}_1 \otimes \hat{S}_{2x},
\end{aligned}$$

where $\mathbf{l} = (l_x, l_y)$, and the summation takes into account the open boundary conditions. As previously advanced, the second equality holds only when we restrict to the single-particle subspace, since the application of the Jordan-Wigner transformation in two dimensions introduces nontrivial phase factors that significantly complicate the representation, ruling out this compact form in the many-body regime. Consequently, a simple mapping to fermionic operators is unattainable, which obstructs a direct extrapolation from single-particle behavior to many-body dynamics via Slater determinants. As

such, it precludes the possibility of obtaining an exact closed form in the many-body regime in dimensions larger than one—Table I summarizes the possible scenarios.

In what follows, to better understand the interplay between dimensionality and interaction effects, we separately analyze the single- and the many-particle cases. For the latter, we rely on approximations and investigate their validity.

A. Single-particle case

Following the same reasoning as in one dimension, we assume that the original Hamiltonian \hat{H}_0 , one of whose eigenstates serves as the initial state for the dynamics, is given by:

$$\begin{aligned}
\hat{H}_0 &= \sum_{\mathbf{l}} (l_x + l_y) \hat{a}_{\mathbf{l}}^\dagger \hat{a}_{\mathbf{l}} \\
&= -\hat{S}_{1z} \otimes \hat{I}_2 - \hat{I}_1 \otimes \hat{S}_{2z} + \left(\frac{L_x + L_y}{2} - 1 \right) \hat{I}_1 \otimes \hat{I}_2. \quad (9)
\end{aligned}$$

Repeating the previous calculations, we obtain the following emergent Hamiltonian,

$$\begin{aligned} \hat{\mathcal{M}}(t) = & \left(\frac{L_x + L_y}{2} - 1 \right) \hat{I}_1 \otimes \hat{I}_2 \\ & + \sin(t) \left(\hat{S}_{1y} \otimes \hat{I}_2 + \hat{I}_1 \otimes \hat{S}_{2y} \right) \\ & - \cos(t) \left(\hat{S}_{1z} \otimes \hat{I}_2 + \hat{I}_1 \otimes \hat{S}_{2z} \right), \quad (10) \end{aligned}$$

where the nested commutators used to compute the infinite series [Eq. (1)] follow the pattern $\hat{\mathcal{H}}_{2n} = -(\hat{S}_{1z} \otimes \hat{I}_2 + \hat{I}_1 \otimes \hat{S}_{2z})$ and $\hat{\mathcal{H}}_{2n+1} = i(\hat{S}_{1y} \otimes \hat{I}_2 + \hat{I}_1 \otimes \hat{S}_{2y})$, for even and odd terms, respectively. This result establishes a direct analogy between the single-particle dynamics of a hard-core boson and that of two noninteracting large spins with spin quantum numbers $s_1 = \frac{(L_x - 1)}{2}$ and $s_2 = \frac{(L_y - 1)}{2}$, respectively. Here, each direction in the original model maps an independent spin, and is a direct generalization of the emergent Hamiltonian for the single-particle version of the 1D case, Eq. (5).

In fact, interactions between these spins can be introduced by incorporating diagonal hopping terms in the original Hamiltonian, by modifying \hat{H}_f as

$$\hat{H}_f = \hat{S}_{1x} \otimes \hat{I}_2 + \hat{I}_1 \otimes \hat{S}_{2x} + \hat{S}_{1x} \otimes \hat{S}_{2x}. \quad (11)$$

This compact representation highlights that the nearest-neighbor hopping amplitudes in this case are $J_{l_\mu} = \frac{1}{2} \sqrt{l_\mu(L_\mu - l_\mu)}$ with $\mu = x, y$ in terms of hard-core boson operators, and that the next-nearest-neighbor amplitudes are $J_l = \frac{1}{4} \sqrt{l_x l_y (L_x - l_x)(L_y - l_y)}$. Within this framework, a convergent emergent Hamiltonian can still be obtained, expressed as [38],

$$\begin{aligned} \hat{\mathcal{M}}(t) = & \left(\frac{L_x + L_y}{2} - 1 \right) \\ & + \sin \left[(1 + \hat{S}_{1x})t \right] \hat{S}_{2y} - \cos \left[(1 + \hat{S}_{1x})t \right] \hat{S}_{2z} \\ & + \hat{S}_{1y} \sin \left[(1 + \hat{S}_{2x})t \right] - \hat{S}_{1z} \cos \left[(1 + \hat{S}_{2x})t \right], \quad (12) \end{aligned}$$

where the nested commutators in this case read $\hat{\mathcal{H}}_{2n} = -[\hat{S}_{1z}(1 + \hat{S}_{2x})^{2n} + (1 + \hat{S}_{1x})^{2n} \hat{S}_{2z}]$ and $\hat{\mathcal{H}}_{2n+1} = i[\hat{S}_{1y}(1 + \hat{S}_{2x})^{2n+1} + (1 + \hat{S}_{1x})^{2n+1} \hat{S}_{2y}]$, which, as before, can be exactly summed in Eq. (1).

Figures 3(a) and 3(b) show the evolution of the half-system entanglement entropy \mathcal{S}_A under the dynamics generated by the Hamiltonian \hat{H}_f in Eqs. (8) and (11), respectively, when taking the initial state as a single excitation in one corner of the lattice, $|\psi(0)\rangle = |\dots 001\rangle$. Here, the partition A is drawn to pick the bottom half of the sites in the lattice. At certain times, $t = t_{\max \mathcal{S}_A} = \pi/2$ for the ‘nearest neighbor’ \hat{H}_f [Eq. (8)] and $t_{\max \mathcal{S}_A} = \pi$ for the ‘next-nearest neighbor one’ [Eq. (11)] [39], the half-system entanglement entropy reaches its maximal value, $\mathcal{S}_A = 1$ (in bits).

These instants correspond to half the time needed to achieve a quantum state transfer, wherein the exci-

tation is transferred to the opposite corner of the lattice [32, 37]. In particular, at maximum entanglement, the state has a distribution over many sites [Figs. 3(c) and 3(d)], in a way to obey inversion symmetry implicit in \hat{H}_f , $\mathbf{l} = (l_x, l_y) \rightarrow (L_x - 1 - l_x, L_y - 1 - l_y) = \mathbf{l}'$, or that the spin projection quantum number along the z axis $m_{1,2} = -s_{1,2}, \dots, s_{1,2}$ for both spins are simultaneously reversed. In this latter mapping, one can interpret the dynamics as the precession of (the expectation values of) spins about the x axis in the Bloch sphere with the same rate [Figs. 3(e) and 3(f)]. While in the nearest neighbor, or noninteracting spins case $\hat{H}_f = \hat{S}_{1x} + \hat{S}_{2x}$, the precession is trivial, it becomes more involved in the presence of interactions [Eq. (11)], yet also accomplishing the quantum state transfer protocol when the trajectory, starting at $+z$ for our initial state reaches the $-z$ -pole of the Bloch sphere [37].

Returning to the analysis of the emergent Hamiltonian, it becomes clear that one can utilize it to freeze the dynamics after accomplishing the quantum state transfer. For instance, the original perfect protocol of quantum state transfer relies on switching off all couplings once the transfer is accomplished. Instead, one can quench the dynamics, $\hat{H}_f \rightarrow \hat{\mathcal{M}}(2t_{\max \mathcal{S}_A})$, since the transferred state is an eigenstate of the emergent Hamiltonian. This is immediately seen for the nearest-neighbor case [Eq. (10)], in which $\hat{\mathcal{M}}(t = \pi) = \left(\frac{L_x + L_y}{2} - 1 \right) + \cos(t) \left(\hat{S}_{1z} + \hat{S}_{2z} \right)$, and the transferred state, $|\psi\rangle = |-z_1\rangle \otimes |-z_2\rangle$, is clearly an eigenstate.

B. Many-particle case

We now extend our analysis to the many-particle case on the 2D lattice, where interactions due to the hard-core constraint significantly complicate the dynamics. Unlike in the single-particle scenario, where we obtained an exact closed-form emergent Hamiltonian, the many-body case presents formidable challenges due to the increasing complexity of the nested commutators in Eq. (1) and the impossibility of mapping the Hamiltonian to that of large spins. This results in the compactness of the emergent Hamiltonian being elusive and necessitating the use of approximate methods to gain meaningful insights.

For example, consider the entangling Hamiltonian

$$\begin{aligned} \hat{H}_f = & \sum_{\mathbf{l}} \frac{\sqrt{l_x(L_x - l_x)}}{2} \left(\hat{a}_{1+\hat{x}}^\dagger \hat{a}_{\mathbf{l}} + \text{H.c.} \right) \\ & + \sum_{\mathbf{l}} \frac{\sqrt{l_y(L_y - l_y)}}{2} \left(\hat{a}_{1+\hat{y}}^\dagger \hat{a}_{\mathbf{l}} + \text{H.c.} \right) \\ & + J_\times \sum_{\mathbf{l}} \left[\left(\hat{a}_{1-\hat{x}+\hat{y}}^\dagger \hat{a}_{\mathbf{l}} + \text{H.c.} \right) \right. \\ & \quad \left. + \left(\hat{a}_{1+\hat{x}+\hat{y}}^\dagger \hat{a}_{\mathbf{l}} + \text{H.c.} \right) \right], \quad (13) \end{aligned}$$

which, unlike previous cases, sets a homogeneous next-

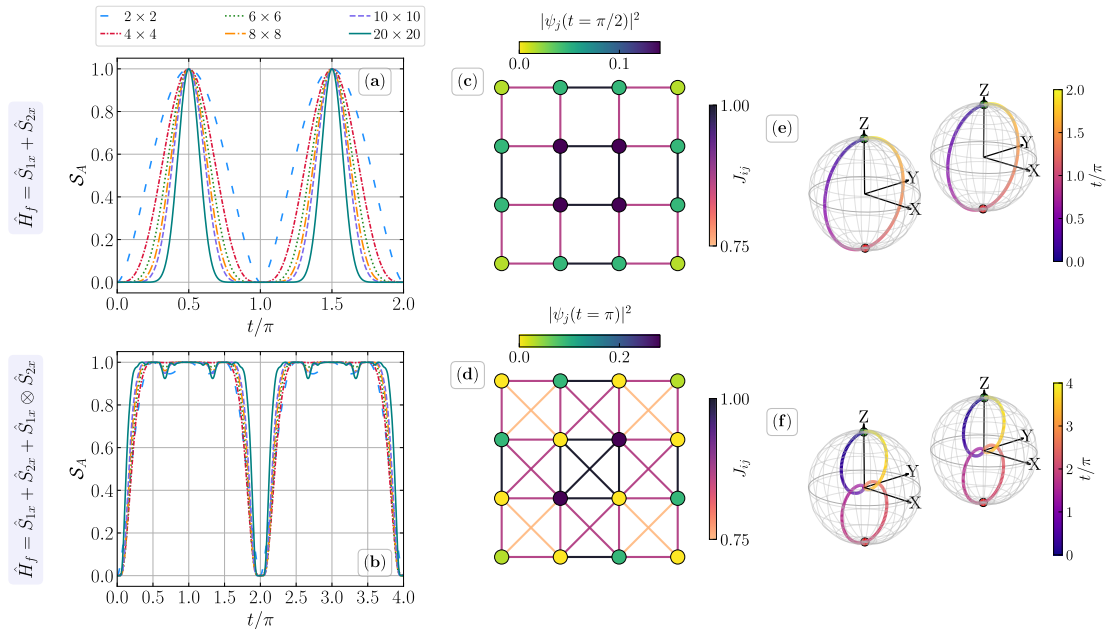


FIG. 3. Dynamics of the half-system entanglement entropy considering different lattice sizes $L_x \times L_y$, for the [next-] nearest-neighbor entangling Hamiltonian (a) [(b)] taking as initial product state $|\psi(0)\rangle$ a single excitation at the lower left corner of the lattice. (c) and (d) Snapshots of the site resolved probabilities $|\psi_j|^2$ at the times where the entanglement entropy is maximal. (e) and (f) Expectation values of $\{\langle \hat{S}_{1\alpha} \rangle\}$ and $\{\langle \hat{S}_{2\alpha} \rangle\}$ ($\alpha = x, y, z$) over time, defining a trajectory in the Bloch sphere—here, the colorbar maps the time t . As indicated, (a), (c), and (e) [(b), (d), and (f)] refer to the entangling Hamiltonian \hat{H}_f in Eq. (8) [(11)].

nearest-neighbor (NNN) hopping, with amplitude J_\times . And, as before, the initial Hamiltonian, one of whose eigenstates serves as the starting point for the dynamics, is given by $\hat{H}_0 = \sum_{\mathbf{l}} (l_x + l_y) \hat{a}_{\mathbf{l}}^\dagger \hat{a}_{\mathbf{l}}$. Summing Eq. (1) does not lead to a closed form, as previously realized in other 1D Hamiltonians [28, 29]. Instead, another approach is to truncate that sum at either first, $\hat{\mathcal{M}}^{(1)}(t) = \hat{H}_0 - i t \hat{\mathcal{H}}_1$, or second orders in time, $\hat{\mathcal{M}}^{(2)}(t) = \hat{H}_0 - i t \hat{\mathcal{H}}_1 - \frac{t^2}{2} \hat{\mathcal{H}}_2$. For sufficiently small times, t can be treated as a perturbative parameter, and truncating at these orders should provide reasonable approximations within short-time dynamics. Notably, with each higher order n , $\hat{\mathcal{M}}^{(n)}(t)$ becomes increasingly nonlocal, spreading across the lattice and appearing structurally complex. The explicit forms of the $\hat{\mathcal{M}}^{(1)}(t)$ and $\hat{\mathcal{M}}^{(2)}(t)$ are provided in Appendix A, where we anticipate that they involve current-density-like terms for $\hat{\mathcal{H}}_1$ and density-assisted hoppings for $\hat{\mathcal{H}}_2$, supplemented by a renormalization of the onsite energies.

To verify their effectiveness, we report in Fig. 4 the normalized overlap between the time-evolved state $|\psi(t)\rangle$ and $\hat{\mathcal{M}}^{(1,2)}(t)|\psi(t)\rangle$, for an initial state consisting of two particles positioned at opposite corners of the $L_x \times L_y$ lattice [40], for $J_\times = 0$. That is, we normalize this overlap by $E_{\hat{\mathcal{M}}} \equiv \|\hat{\mathcal{M}}(t)|\psi(t)\rangle\|$: if $\hat{\mathcal{M}}(t)$ were exact, $\hat{\mathcal{M}}(t)|\psi(t)\rangle$ would be a scalar multiple of $|\psi(t)\rangle$, making the overlap $\langle \psi(t) | \hat{\mathcal{M}}(t) | \psi(t) \rangle / E_{\hat{\mathcal{M}}} = 1$. Since $\hat{\mathcal{M}}(t)$

is an approximation in our case, the deviation of this overlap from one quantifies the accuracy of this approximation, indicating how efficiently $\hat{\mathcal{M}}(t)$ preserves $|\psi(t)\rangle$ at a given time t . Concretely, the normalization would be time independent and equal to the absolute value of the energy associated with the initial state in \hat{H}_0 : $E_{\hat{\mathcal{M}}} = |\langle \psi(t) | \hat{\mathcal{M}} | \psi(t) \rangle| = |\langle \psi(t=0) | \hat{H}_0 | \psi(t=0) \rangle|$, where we make use of the definition of the *exact* emergent Hamiltonian.

The results show that the overlap is close to one at short timescales, as expected, and remains so for longer t when considering the higher-order approximation $\hat{\mathcal{M}}^{(2)}(t)$ instead of $\hat{\mathcal{M}}^{(1)}(t)$ —Figs. 4(a) and 4(b), with the same vertical scale. Furthermore, increasing the system size helps maintain the overlap near one for larger timescales, although it eventually decreases steadily. Additionally, a secondary approach can be used, given the form of our initial state: at short times, one effectively has the dynamics of independent particles, since they are far apart in the lattice. As such, a potentially better emergent Hamiltonian is to take the one for a single particle, in which the spin-mapping is possible, and promote it to the many-body setting—that is, using $\hat{\mathcal{M}}(t)$ in Eq. (10) as a “hopping matrix” and applying it directly to the many-body regime, thereby discarding all nonlocal interactions present in the full emergent Hamiltonian. We refer to this approximation as $\hat{\mathcal{M}}_{\text{spin}}(t)$, owing to the

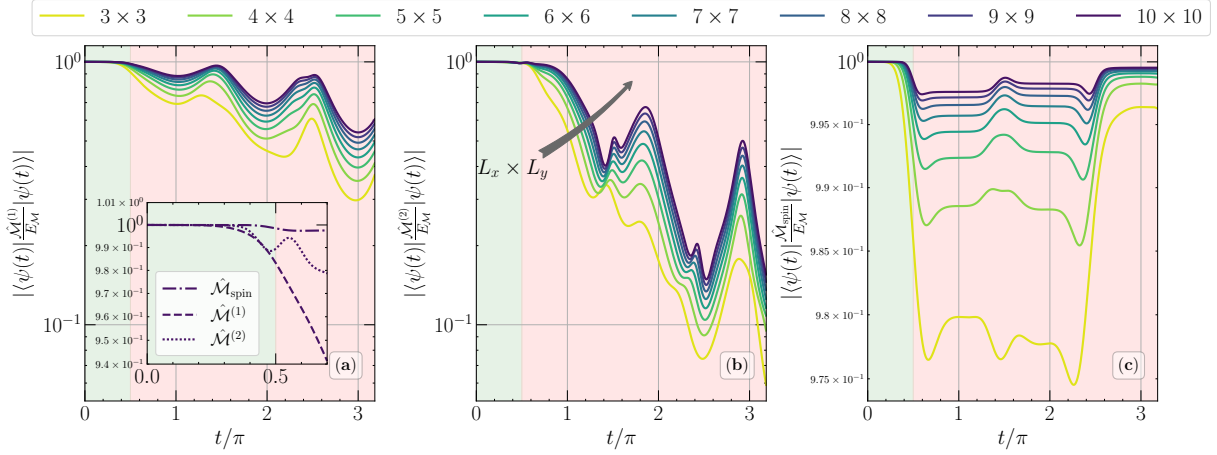


FIG. 4. (a) Time evolution of the overlap between the time-evolved state $|\psi(t)\rangle$ and the normalized $\hat{\mathcal{M}}(t)|\psi(t)\rangle$ under the first-order emergent Hamiltonian $\hat{\mathcal{M}}^{(1)}$ for different system sizes $L_x \times L_y$. The initial state consists of two particles positioned at opposite corners of the square lattice. (b) [(c)] The same, but considering the second-order emergent Hamiltonian $\hat{\mathcal{M}}^{(2)}$ [the spin emergent Hamiltonian $\hat{\mathcal{M}}_{\text{spin}}$]. The inset in (a) contrasts the overlap at short times among the different approximate emergent Hamiltonian for a 10×10 lattice. The shadings in all panels highlight the different regimes where the dynamics are effectively single particle and when such a distinction can no longer be made—see text.

exact spin mapping in the single-particle case.

Remarkably, Fig. 4(c) shows that this approximate emergent Hamiltonian (note the different vertical scale) is substantially more effective in preserving the time-dependent state $|\psi(t)\rangle$ in comparison to low-order truncated ones. One of the reasons for that stems from an

inherent timescale in the problem for this case: Due to the spin mapping in the single-particle case, we expect a periodicity of 2π , implying that a single excitation should take a time 2π to traverse the entire lattice and return. Consequently, it takes approximately π for a particle to travel from one corner to the opposite corner, and $\pi/2$ for two particles initially at opposite corners to effectively “meet”. Thus, for $t \lesssim \pi/2$, the dynamics are in practice single-particle-like, during which $\hat{\mathcal{M}}_{\text{spin}}$ remains a good approximation. Beyond this time, interactions (hard-core constraint) are unavoidable, introducing deviations due to the approximate nature of $\hat{\mathcal{M}}(t)$ —the inset in Fig. 4(a) contrasts the different approximate emergent Hamiltonians at short times, showing how $\hat{\mathcal{M}}_{\text{spin}}$ is more robust in preserving the overlap. This effect is further enhanced in larger lattices, where the picture of independent particles at short times becomes considerably more reliable. Going beyond the two-particle case, we now contrast the effect of a homogeneous J_x in the overlap for the case where one has an initial state with three particles in one corner of the lattice, minimizing $\langle\psi(0)|\hat{H}_0|\psi(0)\rangle$. We focus on the truncated second-order emergent Hamiltonian $\hat{\mathcal{M}}^{(2)}(t)$, since no approximate direct mapping to a spin-like emergent Hamiltonian is possible, and, due to the nature of our initial state, the hard-core constraint sets in right from the start. The larger the number of hopping terms in \hat{H}_f , the more likely it is that a low-order truncation $\hat{\mathcal{M}}^{(n)}(t)$ would not preserve the state—this can be understood in terms of additional corrections the n -order emergent Hamiltonian would exhibit, leading to an effectively poor approximation.

This is indeed observed in Fig. 5(a), where the overlap systematically decays from one at shorter times as J_x is increased. In fact, since some of these corrections lead

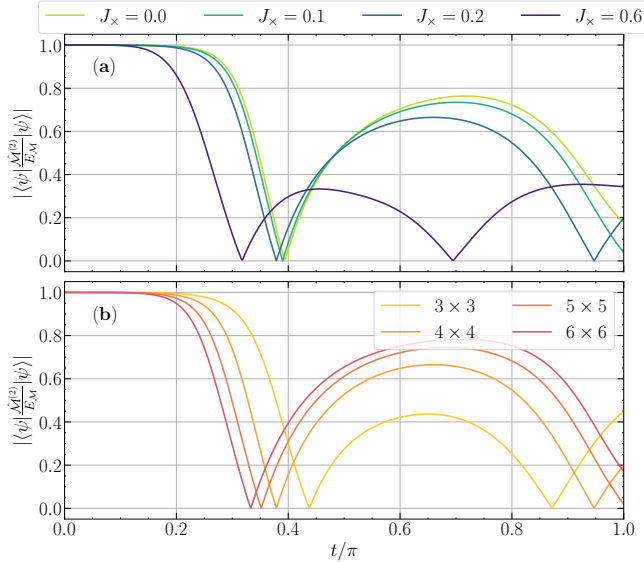


FIG. 5. (a) Comparison of the overlap between $|\psi(t)\rangle$ and the normalized $\hat{\mathcal{M}}(t)|\psi(t)\rangle$ under the second-order emergent Hamiltonian $\hat{\mathcal{M}}^{(2)}$, for different diagonal hoppings J_x in \hat{H}_f , on a 6×6 lattice. The initial state consists of three particles at the lower corner of the square lattice, specifically at sites $(0, 0)$, $(1, 0)$, and $(0, 1)$. (b) The same as in (a), but contrasting different system sizes for $J_x = 0.2$.

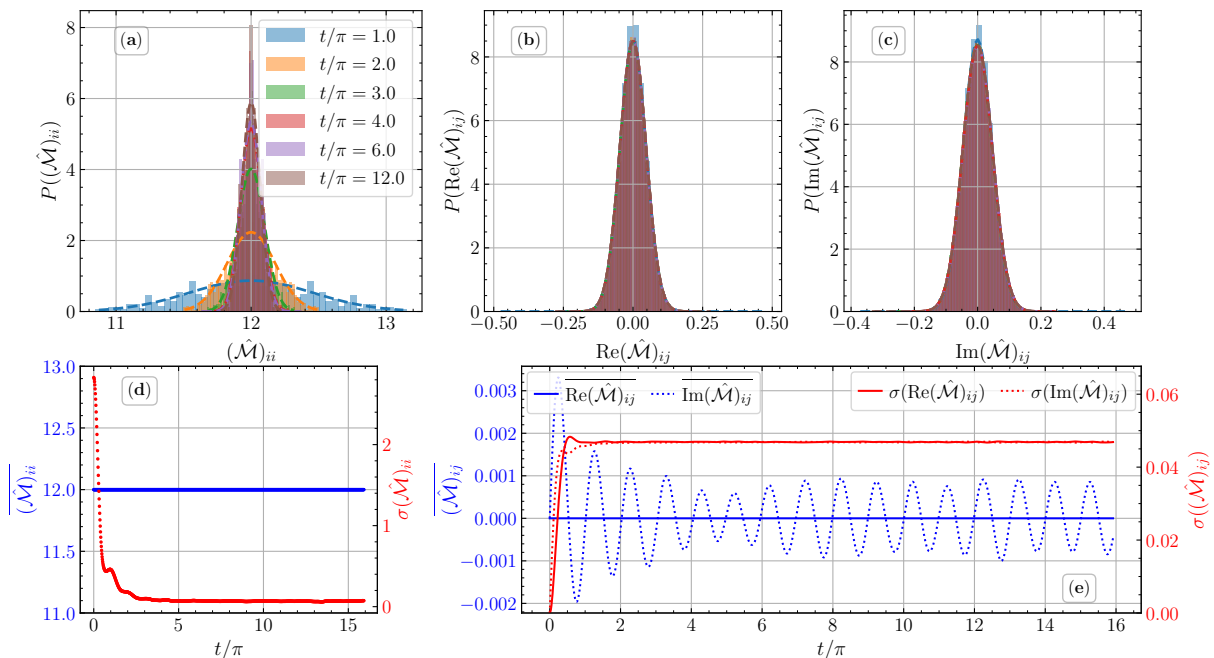


FIG. 6. Probability density of occurrence of the emergent Hamiltonian $\hat{\mathcal{M}}(t)$ matrix elements in the Fock basis: (a) diagonal elements, and the (b) real and (c) imaginary parts of the off-diagonal elements at different time stamps; Gaussian fittings are shown with dashed lines. (d) and (e) Dynamics of the mean and standard deviation of the fitted Gaussian for the diagonal (d) and off-diagonal (e) matrix elements. All data refer to the exact $\hat{\mathcal{M}}(t)$ for the model in Eq. (13) with $\hat{H}_0 = \sum_1 (l_x + l_y) \hat{a}_1^\dagger \hat{a}_1$ on a 4×4 lattice with three excitations and a constant diagonal hopping amplitude $J_\times = 0.6$.

to a renormalization of the onsite energies, the larger the lattice, the worse one would expect that $\hat{\mathcal{M}}^{(n)}$ would fare in storing the time-dependent state, as is indeed observed in Fig. 5(b).

IV. SPECTRAL ANALYSIS

As we have noted, the emergent Hamiltonian is, by definition, a unitary transformation of \hat{H}_0 :

$$\hat{\mathcal{M}}(t) = \hat{U} \hat{H}_0 \hat{U}^\dagger, \quad (14)$$

where $\hat{U} \equiv e^{-i\hat{H}_f t}$ at a given time t . This ensures that the eigenvalues of $\hat{\mathcal{M}}(t)$ are identical to those of \hat{H}_0 . Since \hat{H}_0 is clearly integrable for the cases we have investigated so far, $\hat{\mathcal{M}}(t)$ does not exhibit any chaotic behavior as identified by the emergence of level repulsion [41–43]. In fact, for our choice of \hat{H}_0 , the eigenvalues are evenly spaced with integer-valued gaps.

Despite this, the structure of $\hat{\mathcal{M}}(t)$ becomes increasingly non-local as higher-order terms in its nested commutator expansion are included. These terms include density-assisted hoppings (see Appendix A) for second order, for example, where the hopping amplitude depends on the occupation of additional sites. With each successive order, the range of sites contributing to this effect extends further. This behavior arises directly from the hard-core constraint, distinguishing the system from

free bosons or fermions. In general, the commutator of two quadratic terms composed solely of free bosonic or fermionic creation and annihilation operators remains quadratic, preventing the emergence of density-assisted (four-body or higher) terms [44]. However, the hard-core constraint introduces strong interactions, leading to the formation of these inherently nonlocal terms.

As additional terms are incorporated, $\hat{\mathcal{M}}(t)$ becomes increasingly dense, raising the suspicion that it may effectively resemble a random matrix. In the infinite-order limit (for any finite t), $\hat{\mathcal{M}}(t)$ is highly nonsparse and appears “random.” This appearance is, however, misleading: $\hat{\mathcal{M}}(0) = \hat{H}_0$ is diagonal in the Fock basis, and the growth of nonlocal terms with time merely creates the semblance of randomness. Because $\hat{\mathcal{M}}(t)$ is unitarily similar to \hat{H}_0 (and thus Hermitian with the same eigenvalues), the spectrum remains highly regular and does not exhibit Wigner-Dyson level repulsion. This dichotomy between random-matrix-like structure without level repulsion is explored in Fig. 6, where we examine histograms of the matrix elements of the numerically exact emergent Hamiltonian $\hat{\mathcal{M}}(t)$ [Eq. (14)] at different time stamps. This is constructed for \hat{H}_f in Eq. (13), and $\hat{H}_0 = \sum_1 (l_x + l_y) \hat{a}_1^\dagger \hat{a}_1$ for the three excitation subspace.

We start with the (normalized) histograms of diagonal elements [Fig. 6(a)], which are real, where they rapidly develop a Gaussian structure, overcoming the structured pattern associated with \hat{H}_0 at short times. Notably, the

mean is time independent, a direct consequence of the trace conservation under unitary transformations. Meanwhile, such a Gaussian structure exhibits a standard deviation that equilibrates to a saturation value [Fig. 6(d)]. In turn, for off-diagonal elements [the real and imaginary parts, Fig. 6(b) and 6(c), respectively], the pattern is similar, but their mean hovers around zero, and the standard deviation quickly grows from zero to an equilibrium value [Fig. 6(e)].

To characterize the similarity of $\hat{\mathcal{M}}(t)$ to a random matrix at large t , we quantify the fluctuations of matrix elements by the ratio $r \equiv \sigma_{\text{off}}/\sigma_{\text{diag}}$, where σ_{off} denotes the standard deviation of the off-diagonal elements and σ_{diag} that of the diagonal elements. Numerically, the real and imaginary parts of the off-diagonal elements coincide ($\sigma_{\text{off}}^{\text{real}} \simeq \sigma_{\text{off}}^{\text{imag}}$), thus we treat them jointly. For the 4×4 example in Fig. 6, we find a representative late-time value $r \approx 0.63$, consistent across the sampled time stamps. Across system sizes and fillings f , and excluding two dilute-filling outliers ($5 \times 5, f = 3/25 = 0.125$ and $5 \times 5, f = 0.08$), the ratio has mean $\bar{r} = 0.662$ with sample standard deviation 0.029, spanning the range 0.616-0.697. At first sight, they look suspiciously close to random-matrix expectations. For comparison, a Gaussian ensemble within random matrix theory (RMT), with standard normalization, gives $r_{\text{RMT}} = 1/\sqrt{2} \approx 0.707$ [43]. Our slightly lower values are plausibly explained by the finite Hilbert spaces accessible here and by residual symmetries such as particle-hole symmetry that constrain the matrix elements. Even though the emergent Hamiltonian is dense and includes most nonlocal terms, it is still a unitary transformation of \hat{H}_0 rather than a draw from an independent Gaussian ensemble.

V. ANOTHER EXAMPLE: STORING A GHZ STATE

We now move on to yet another example of using the emergent Hamiltonian protocol aimed at preparing and storing a GHZ state, which exhibits fragile, globally distributed entanglement. Such correlations are effectively impossible to maintain in MBL-like protocols, which tend to drive the system toward a classical mixture of its macroscopic branches due to their inherent locality. In the context of quantum circuits, Ref. [45] shows that, in place of the conventional $O(N)$ -depth CNOT ladder used for GHZ generation, a constant-depth $O(1)$ can be realized through a single collective entangling operation combined with global rotations (i.e., all-to-all couplings among qubits) and parallel parity readout for verification. When coupled with our emergent Hamiltonian protocol, which freezes the complete state including its global correlations, this approach provides a direct route to preparing and storing GHZ states.

Following Refs. [45–47], we focus on the collective “one-axis twisting” (OAT) setting, also emulated with trapped

atoms [48], where the entangling Hamiltonian is [49]

$$\hat{H}_{\text{OAT}} = -\lambda \hat{S}_z^2. \quad (15)$$

We restrict the dynamics to the totally symmetric spin sector of L qubits, $s = L/2$, where the Dicke basis states $\{|s m\rangle\}$ are defined as eigenstates of the global spin operators

$$\hat{S}^2 |s m\rangle = s(s+1) |s m\rangle \quad \text{and} \quad \hat{S}_z |s m\rangle = m |s m\rangle, \quad (16)$$

with $m = -s, -s+1, \dots, s$. We start from the spin-coherent state aligned along the $-y$ axis in the Bloch sphere,

$$|\psi(0)\rangle = \left(\frac{|0\rangle - i|1\rangle}{\sqrt{2}} \right)^{\otimes L}, \quad (17)$$

or, equivalently, in the Dicke basis,

$$|\psi(0)\rangle = \sum_{m=-s}^s c_m |m\rangle, \quad c_m = 2^{-L/2} (-i)^{m+s} \sqrt{\binom{L}{m+s}}, \quad (18)$$

which is an eigenstate of $\hat{H}_0 = \hat{S}_y$. What we aim to show is that an emergent Hamiltonian $\hat{\mathcal{M}}(t) = e^{-i\hat{H}_{\text{OAT}}t} \hat{S}_y e^{+i\hat{H}_{\text{OAT}}t} = e^{+i\lambda \hat{S}_z^2 t} \hat{S}_y e^{-i\lambda \hat{S}_z^2 t}$ has a closed form that can be used to freeze desired states. In particular, within the subspace defined by $\{|m\rangle\}$, this can be simplified by decomposing \hat{S}_y into the spin ladder operators, $\hat{S}_y = \frac{\hat{S}_+ - \hat{S}_-}{2i}$, and noticing that $e^{+i\lambda \hat{S}_z^2 t} \hat{S}_\pm e^{-i\lambda \hat{S}_z^2 t} |m\rangle = e^{i\lambda t[(m\pm 1)^2 - m^2]} \hat{S}_\pm |m\rangle = e^{i\lambda t(\pm 2m+1)} \hat{S}_\pm |m\rangle$. As a result, the emergent Hamiltonian assumes a compact form,

$$\hat{\mathcal{M}}(t) = \frac{1}{2i} \left[e^{i\lambda t(2\hat{S}_z+1)} \hat{S}_+ - e^{-i\lambda t(2\hat{S}_z-1)} \hat{S}_- \right]. \quad (19)$$

Alternatively, we can also use the finite matrix elements of the operators in the $\{|m\rangle\}$ basis, $(S_z)_{mm} = m$ and $(S_\pm)_{m,m\pm 1} = \sqrt{s(s+1) - m(m\pm 1)}$, to write the matrix elements of the emergent Hamiltonian as

$$\left(\hat{\mathcal{M}}(t) \right)_{m,m\pm 1} = \mp \frac{1}{2i} e^{\mp i\lambda t(2m\pm 1)} \sqrt{s(s+1) - m(m\pm 1)} \quad (20)$$

This makes it explicit that $\hat{\mathcal{M}}(t)$ is tridiagonal in the Dicke basis, and to note that the m -dependent phases $e^{\pm i\lambda t(2m\pm 1)}$ appearing in $\hat{\mathcal{M}}(t)$ become particularly simple at special times.

For instance, at $t = \pi/(2\lambda)$, one finds $e^{i(\pi/2)(2m+1)} = i(-1)^m$, producing an alternating sign pattern between neighboring Dicke sectors. This “staggered hopping” frustrates intermediate m -values, leading to an eigenstate that approaches a GHZ state, for large L , along the y -axis on the equator,

$$\begin{aligned} |\text{GHZ}_\phi^y\rangle &= \frac{|0_y \dots 0_y\rangle + e^{i\phi} |1_y \dots 1_y\rangle}{\sqrt{2}} \\ &= \hat{R}_x(-\pi/2) |\text{GHZ}_\phi\rangle, \end{aligned} \quad (21)$$

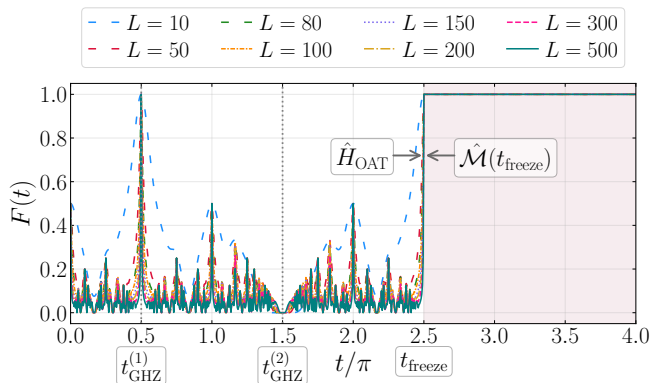


FIG. 7. Fidelity $F(t) = |\langle \text{GHZ}_{3\pi/2} | R_x(-\pi/2) \psi(t) \rangle|^2$ between the rotated state $R_x(-\pi/2) |\psi(t)\rangle$ and the target GHZ at $t_{\text{GHZ}}^{(1)} = \pi/(2\lambda)$ for various L . The dotted lines indicate $t_{\text{GHZ}}^{(1,2)}$.

where $|\text{GHZ}_\phi\rangle$ is the symmetric superposition of the $m = \pm s$ states, and $R_x(\theta)$ a global rotation about the x -axis by θ . At $t = \pi/\lambda$, on the other hand, all phases align ($e^{i\pi(2m+1)} = -1$), recovering the original \hat{S}_y up to a global sign and reviving the initial spin-coherent state. These special times thus correspond to the well-known “cat-state” and “revival” points of the one-axis twisting dynamics [45, 48] and demonstrate why $\hat{\mathcal{M}}(t)$ can be used to freeze a macroscopically entangled GHZ-like state.

Let us now show how the protocol works in practice. By setting $\lambda = 1$, at times $t_{\text{GHZ}}^{(1)} = \pi/2$ (modulo 2π), the evolution produces the GHZ state

$$|\psi(t = \pi/2)\rangle = |\text{GHZ}_{\phi=3\pi/2}\rangle = \frac{1}{\sqrt{2}} (|0\dots 0\rangle - i|1\dots 1\rangle), \quad (22)$$

while at times $t_{\text{GHZ}}^{(2)} = 3\pi/2$ (modulo 2π) it yields another GHZ state

$$|\psi(t = 3\pi/2)\rangle = |\text{GHZ}_{\phi=\pi/2}\rangle = \frac{1}{\sqrt{2}} (|0\dots 0\rangle + i|1\dots 1\rangle). \quad (23)$$

These two GHZ states differ by the relative phase $\pm i$ between the $|0\dots 0\rangle$ and $|1\dots 1\rangle$ components and are mutually orthogonal.

Because the GHZ produced via this protocol naturally lies along the y direction of the collective Bloch sphere, we rotate the time-evolved state $|\psi(t)\rangle$ about the x axis by $-\pi/2$ to map the equatorial GHZ to the computational GHZ state before calculating the fidelity:

$$F(t) = \left| \langle \text{GHZ}_\phi | \hat{R}_x(-\pi/2) \psi(t) \rangle \right|^2. \quad (24)$$

Figure 7 shows the fidelity dynamics generated by \hat{H}_{OAT} starting from the $-y$ -oriented spin coherent state, $|1_y\rangle^{\otimes L}$ for different numbers of qubits L . The curve peaks at $t_{\text{GHZ}}^{(1)}$ modulo 2π , where the GHZ forms. To attest the efficiency of our quantum memory protocol, we quench

the dynamics at time $t_{\text{freeze}} = t_{\text{GHZ}}^{(1)} + 2\pi$ by switching its generator from \hat{H}_{OAT} to the emergent Hamiltonian $\hat{\mathcal{M}}(t_{\text{freeze}})$, thus freezing this globally distributed entangled state indefinitely.

VI. SUMMARY AND OUTLOOK

The quest to store highly entangled quantum states, thereby realizing a robust quantum memory, is one of the fundamental cornerstones of the quantum computing paradigm. In this work, we have demonstrated that the protocol of emergent Hamiltonians can achieve this goal in several contexts, in particular for stabilizing entangled states such as tensor products of Bell states or GHZ states. The essential ingredient is the focus on compact emergent Hamiltonians, which can be readily implemented within existing quantum computing platforms.

In situations where no compact form exists, such as in the many-body regime in more than one dimension, approximate emergent Hamiltonians can be derived to freeze the corresponding entangled state after an initial short dynamics effectively. From a mathematical perspective, we further revealed that such Hamiltonians inherit quantum chaotic features: while they arise from simple parent Hamiltonians with non-entangled eigenstates, their unitary transformation often generates dense operator structures reminiscent of chaotic systems. In this sense, their matrix properties align with the corresponding random matrix class, even though their spectra do not display level repulsion, distinguishing them from genuinely chaotic ensembles.

An intriguing direction for future exploration concerns ergodicity. The eigenstate thermalization hypothesis (ETH) asserts that the expectation values of few-body observables in energy eigenstates are smooth functions of the eigenenergy, with eigenstate-to-eigenstate fluctuations that vanish exponentially with system size [43, 50, 51]. Whether generic emergent Hamiltonians satisfy ETH remains an open question. A key subtlety is that a local observable in the original basis may be mapped to a highly nonlocal one under the unitary transformation defining $\hat{\mathcal{M}}(t)$, thereby evading the conventional ETH framework. Systematic tests across a large class of emergent Hamiltonians could clarify the extent to which ergodicity and ETH hold (or fail) in this setting.

Finally, concerning experimental explorations, one limiting characteristic of actual devices is the inherent presence of decoherence, which can ultimately spoil the ideal quantum memory enabled by the emergent Hamiltonian. Incoherent processes such as relaxation and dephasing progressively suppress phase coherence and redistribute population, thereby degrading eigenstates of $\hat{\mathcal{M}}(t)$. A quantitative analysis of these effects for the GHZ case is presented in Appendix B.

Nonetheless, *coherent* scrambling arising from imperfect control or residual interactions is expected to occur on a time scale that scales inversely with the energy gap.

Since these gaps can be tuned through appropriate manipulation of the parent Hamiltonian \hat{H}_0 , one can prolong the operational memory window: large spectral gaps intrinsically suppress coherent (unitary) perturbations by energetically isolating the target eigenstate.

It is worth emphasizing that the emergent-Hamiltonian framework naturally acts as a design toolbox: the parent Hamiltonian \hat{H}_0 fixes the eigenspectrum, while the driving Hamiltonian \hat{H}_f shapes the dynamics. This two-Hamiltonian structure enables one to engineer both preparation and storage of entangled states, ensuring that a desired state can be made an eigenstate of \hat{H}_0 and stabilized against coherent perturbations. In this way, the framework provides a flexible and experimentally relevant route toward the controlled realization of long-lived quantum memories.

ACKNOWLEDGMENTS

R.M. acknowledges support from the T_cSUH Welch Professorship Award. Numerical simulations were per-

formed with resources provided by the Research Computing Data Core at the University of Houston. This work also used TAMU ACES at Texas A&M HPRC through allocation PHY240046 from the Advanced Cyberinfrastructure Coordination Ecosystem: Services & Support (ACCESS) program, which is supported by U.S. National Science Foundation grants 2138259, 2138286, 2138307, 2137603, and 2138296.

DATA AVAILABILITY

The data that support the findings of this article are openly available [52], embargo periods may apply.

-
- [1] R. Nandkishore and D. A. Huse, Many-body localization and thermalization in quantum statistical mechanics, *Annual Review of Condensed Matter Physics* **6**, 15 (2015).
- [2] F. Alet and N. Laflorencie, Many-body localization: An introduction and selected topics, *Comptes Rendus. Physique* **19**, 498 (2018).
- [3] D. A. Abanin, E. Altman, I. Bloch, and M. Serbyn, Colloquium: Many-body localization, thermalization, and entanglement, *Rev. Mod. Phys.* **91**, 021001 (2019).
- [4] P. Sierant, M. Lewenstein, A. Scardicchio, L. Vidmar, and J. Zakrzewski, Many-body localization in the age of classical computing*, *Reports on Progress in Physics* **88**, 026502 (2025).
- [5] J. Smith, A. Lee, P. Richerme, B. Neyenhuis, P. W. Hess, P. Hauke, M. Heyl, D. A. Huse, and C. Monroe, Many-body localization in a quantum simulator with programmable random disorder, *Nature Physics* **12**, 907 (2016).
- [6] E. K. Carlson, Many-body localized states inch toward equilibrium, *Physics* **13**, s80 (2020), published June 16, 2020; accessed 2025-07-08.
- [7] E. Levi, M. Heyl, I. Lesanovsky, and J. P. Garrahan, Robustness of many-body localization in the presence of dissipation, *Phys. Rev. Lett.* **116**, 237203 (2016).
- [8] M. H. Fischer, M. Maksymenko, and E. Altman, Dynamics of a many-body-localized system coupled to a bath, *Phys. Rev. Lett.* **116**, 160401 (2016).
- [9] H. P. Lüschen, P. Bordia, S. S. Hodgman, M. Schreiber, S. Sarkar, A. J. Daley, M. H. Fischer, E. Altman, I. Bloch, and U. Schneider, Signatures of many-body localization in a controlled open quantum system, *Phys. Rev. X* **7**, 011034 (2017).
- [10] M. Schreiber, S. S. Hodgman, P. Bordia, H. P. Lüschen, M. H. Fischer, R. Vosk, E. Altman, U. Schneider, and I. Bloch, Observation of many-body localization of interacting fermions in a quasirandom optical lattice, *Science* **349**, 842 (2015).
- [11] J. yoon Choi, S. Hild, J. Zeiher, P. Schauß, A. Rubio-Abadal, T. Yefsah, V. Khemani, D. A. Huse, I. Bloch, and C. Gross, Exploring the many-body localization transition in two dimensions, *Science* **352**, 1547 (2016).
- [12] T. Kohlert, S. Scherg, X. Li, H. P. Lüschen, S. Das Sarma, I. Bloch, and M. Aidelsburger, Observation of many-body localization in a one-dimensional system with a single-particle mobility edge, *Phys. Rev. Lett.* **122**, 170403 (2019).
- [13] Q. Guo, C. Cheng, Z.-H. Sun, Z. Song, H. Li, Z. Wang, W. Ren, H. Dong, D. Zheng, Y.-R. Zhang, R. Mondaini, H. Fan, and H. Wang, Observation of energy-resolved many-body localization, *Nature Physics* **17**, 234 (2021).
- [14] S. Scherg, T. Kohlert, P. Sala, F. Pollmann, B. Hebbe Madhusudhana, I. Bloch, and M. Aidelsburger, Observing non-ergodicity due to kinetic constraints in tilted fermi-hubbard chains, *Nature Communications* **12**, 4490 (2021).
- [15] Q. Guo, C. Cheng, H. Li, S. Xu, P. Zhang, Z. Wang, C. Song, W. Liu, W. Ren, H. Dong, R. Mondaini, and H. Wang, Stark many-body localization on a superconducting quantum processor, *Phys. Rev. Lett.* **127**, 240502 (2021).
- [16] W. Morong, F. Liu, P. Becker, K. S. Collins, L. Feng, A. Kyprianidis, G. Pagano, T. You, A. V. Gorshkov, and C. Monroe, Observation of Stark many-body localization without disorder, *Nature* **599**, 393 (2021).
- [17] J. H. Bardarson, F. Pollmann, and J. E. Moore, Unbounded growth of entanglement in models of many-body localization, *Phys. Rev. Lett.* **109**, 017202 (2012).
- [18] M. Serbyn, Z. Papić, and D. A. Abanin, Universal slow growth of entanglement in interacting strongly disordered systems, *Phys. Rev. Lett.* **110**, 260601 (2013).

- [19] A. Nanduri, H. Kim, and D. A. Huse, Entanglement spreading in a many-body localized system, *Phys. Rev. B* **90**, 064201 (2014).
- [20] Beyond the intrinsic limitation that MBL protects only local information, its stability itself is under active scrutiny. Numerical work reports slow many-body delocalization beyond one spatial dimension and a localization threshold that drifts with system size, consistent with the absence of stable MBL in two dimensions in the thermodynamic limit [53, 54]. Even in one dimension, rare thermal inclusions can seed avalanche mechanisms leading to slow but persistent thermalization [55], and monitored dynamics can destabilize prethermal localization regimes [56]. These considerations further motivate disorder-free approaches that freeze the full many-body state by construction.
- [21] P. W. Shor, Scheme for reducing decoherence in quantum computer memory, *Phys. Rev. A* **52**, R2493 (1995).
- [22] E. Knill and R. Laflamme, Theory of quantum error-correcting codes, *Phys. Rev. A* **55**, 900 (1997).
- [23] E. Dennis, A. Kitaev, A. Landahl, and J. Preskill, Topological quantum memory, *Journal of Mathematical Physics* **43**, 4452 (2002).
- [24] A. G. Fowler, M. Mariantoni, J. M. Martinis, and A. N. Cleland, Surface codes: Towards practical large-scale quantum computation, *Phys. Rev. A* **86**, 032324 (2012).
- [25] B. M. Terhal, Quantum error correction for quantum memories, *Rev. Mod. Phys.* **87**, 307 (2015).
- [26] M. Silveri and T. Orell, Many-qubit protection-operation dilemma from the perspective of many-body localization, *Nature Communications* **13**, 5825 (2022).
- [27] A. Nico-Katz, N. Keenan, and J. Goold, Can quantum computers do nothing?, *npj Quantum Information* **10**, 124 (2024).
- [28] L. Vidmar, D. Iyer, and M. Rigol, Emergent eigenstate solution to quantum dynamics far from equilibrium, *Phys. Rev. X* **7**, 021012 (2017).
- [29] Y. Zhang, L. Vidmar, and M. Rigol, Emergent eigenstate solution for generalized thermalization, *Phys. Rev. A* **104**, L031303 (2021).
- [30] Additionally, they exhibit mixed commutation relations, commuting at different sites, $[\hat{a}_i, \hat{a}_j^\dagger] = 0$, while anticommute on the same site, $\{\hat{a}_i, \hat{a}_i^\dagger\} = 1$.
- [31] T. Matsubara and H. Matsuda, A lattice model of liquid helium, I, *Progress of Theoretical Physics* **16**, 569 (1956).
- [32] M. Christandl, N. Datta, A. Ekert, and A. J. Landahl, Perfect state transfer in quantum spin networks, *Phys. Rev. Lett.* **92**, 187902 (2004).
- [33] C. Albanese, M. Christandl, N. Datta, and A. Ekert, Mirror inversion of quantum states in linear registers, *Phys. Rev. Lett.* **93**, 230502 (2004).
- [34] We compute the entanglement entropy via the correlation matrix of free fermions for the relevant partition, as illustrated in Ref. [57].
- [35] That is, starting from $|00\rangle$ through a Hadamard gate on the first qubit, a controlled-NOT on the pair, an X gate on the second qubit, and a subsequent phase gate S on the second qubit [58].
- [36] F. Arute, K. Arya, R. Babbush, D. Bacon, J. C. Bardin, R. Barends, R. Biswas, S. Boixo, F. G. S. L. Brandao, D. A. Buell, B. Burkett, Y. Chen, Z. Chen, B. Chiaro, R. Collins, W. Courtney, A. Dunsworth, E. Farhi, B. Foxen, A. Fowler, C. Gidney, M. Giustina, R. Graff, K. Guerin, S. Habegger, M. P. Harrigan, M. J. Hartmann, A. Ho, M. Hoffmann, T. Huang, T. S. Humble, S. V. Isakov, E. Jeffrey, Z. Jiang, D. Kafri, K. Kechedzhi, J. Kelly, P. V. Klimov, S. Knysh, A. Korotkov, F. Kostritsa, D. Landhuis, M. Lindmark, E. Lucero, D. Lyakh, S. Mandrà, J. R. McClean, M. McEwen, A. Megrant, X. Mi, K. Michielsen, M. Mohseni, J. Mutus, O. Naaman, M. Neeley, C. Neill, M. Y. Niu, E. Ostby, A. Petukhov, J. C. Platt, C. Quintana, E. G. Rieffel, P. Roushan, N. C. Rubin, D. Sank, K. J. Satzinger, V. Smelyanskiy, K. J. Sung, M. D. Trevithick, A. Vainsencher, B. Villalonga, T. White, Z. J. Yao, P. Yeh, A. Zalcman, H. Neven, and J. M. Martinis, Quantum supremacy using a programmable superconducting processor, *Nature* **574**, 505 (2019).
- [37] L. Xiang, J. Chen, Z. Zhu, Z. Song, Z. Bao, X. Zhu, F. Jin, K. Wang, S. Xu, Y. Zou, H. Li, Z. Wang, C. Song, A. Yue, J. Partridge, Q. Guo, R. Mondaini, H. Wang, and R. T. Scalettar, Enhanced quantum state transfer by circumventing quantum chaotic behavior, *Nature Communications* **15**, 4918 (2024).
- [38] Here, we simplify the notation by omitting tensor products, which are obvious in the context.
- [39] The period difference depends only on whether L_x or L_y is even: mapping to large spins $s_i = (L_i - 1)/2$ makes s_i half-integer whenever L_i is even. In the $\hat{S}_{i,x}$ eigenbasis, with $m_i = -s_i, -s_i + 1, \dots, s_i$ (unit spacing), the spectrum is $E = m_1 + m_2$ in the nearest-neighbor case and $E = m_1 + m_2 + m_1 m_2$ in the next-nearest case. The recurrence time (ignoring any overall phase) is set by the fundamental spacing of energy gaps g , i.e., the positive number for which every difference $E - E'$ is an integer multiple of g (here this equals the smallest nonzero gap). For the nearest-neighbor case the gap set is \mathbb{Z} , so $g = 1$ and the period is 2π . For the next-nearest case, shifting $m_1 \rightarrow m_1 + 1$ gives $\Delta E = 1 + m_2$. Thus, the gap set is \mathbb{Z} if both spins are integer (both L_x, L_y odd), but becomes $\mathbb{Z} + \frac{1}{2}$ as soon as one spin is half-integer (i.e., at least one of L_x, L_y is even). So the period is 2π in the former ($g = 1$) and 4π in the latter ($g = \frac{1}{2}$). At 4π the evolution adds a global phase (with respect to the initial state) of -1 , so observables already recur, while the unitary returns to identity only at 8π . For the nearest-neighbor case, it already returns at 2π .
- [40] Alternatively, one often employs a different metric for the measure of the appropriateness of $\hat{\mathcal{M}}^{(n)}(t)$ as an accurate emergent Hamiltonian, such as computing the overlap of the desired eigenstate of the latter with the time-evolved state: $|\langle \Psi_t | \psi(t) \rangle|$ [28, 29]. This is facilitated by the fact that, as a unitary transformation of \hat{H}_0 , $\hat{\mathcal{M}}(t)$ preserves its spectrum. In our case, owing to the form of $\hat{H}_0 = \sum_1 (l_x + l_y) \hat{a}_1^\dagger a_1$, and the chosen initial state $|\psi(0)\rangle$, a symmetric excitation of two excitations at opposite corners of the lattice, there is an extensive degeneracy, complicating the task of monitoring the overlap by inspecting the corresponding eigenvalue to infer what $|\Psi_t\rangle$ is.
- [41] V. Oganesyan and D. A. Huse, Localization of interacting fermions at high temperature, *Phys. Rev. B* **75**, 155111 (2007).
- [42] Y. Y. Atas, E. Bogomolny, O. Giraud, and G. Roux, Distribution of the ratio of consecutive level spacings in random matrix ensembles, *Phys. Rev. Lett.* **110**, 084101 (2013).

- [43] L. D'Alessio, Y. Kafri, A. Polkovnikov, and M. Rigol, From quantum chaos and eigenstate thermalization to statistical mechanics and thermodynamics, *Advances in Physics* **65**, 239 (2016).
- [44] This can be immediately seen for the case of fermions (\hat{c} and \hat{c}^\dagger operators) or bosons (\hat{b} and \hat{b}^\dagger operators), where $[\hat{a}_i^\dagger \hat{a}_j, \hat{a}_k^\dagger \hat{a}_\ell] = \delta_{jk} \hat{a}_i^\dagger \hat{a}_\ell - \delta_{i\ell} \hat{a}_k^\dagger \hat{a}_j$, where $\hat{a}_i = \hat{c}_i$ or \hat{b}_i . For hard-core bosons, on the other hand, this commutator leads to $[\hat{a}_i^\dagger \hat{a}_j, \hat{a}_k^\dagger \hat{a}_\ell] = \delta_{jk} \hat{a}_i^\dagger (1 - 2\hat{n}_j) \hat{a}_\ell - \delta_{i\ell} \hat{a}_k^\dagger (1 - 2\hat{n}_i) \hat{a}_j$.
- [45] C. Song, K. Xu, H. Li, Y.-R. Zhang, X. Zhang, W. Liu, Q. Guo, Z. Wang, W. Ren, J. Hao, H. Feng, H. Fan, D. Zheng, D.-W. Wang, H. Wang, and S.-Y. Zhu, Generation of multicomponent atomic Schrödinger cat states of up to 20 qubits, *Science* **365**, 574 (2019).
- [46] K. Xu, Z.-H. Sun, W. Liu, Y.-R. Zhang, H. Li, H. Dong, W. Ren, P. Zhang, F. Nori, D. Zheng, H. Fan, and H. Wang, Probing dynamical phase transitions with a superconducting quantum simulator, *Science Advances* **6**, eaba4935 (2020).
- [47] K. Xu, Y.-R. Zhang, Z.-H. Sun, H. Li, P. Song, Z. Xiang, K. Huang, H. Li, Y.-H. Shi, C.-T. Chen, X. Song, D. Zheng, F. Nori, H. Wang, and H. Fan, Metrological characterization of non-gaussian entangled states of superconducting qubits, *Phys. Rev. Lett.* **128**, 150501 (2022).
- [48] C. Gross, T. Zibold, E. Nicklas, J. Estève, and M. K. Oberthaler, Nonlinear atom interferometer surpasses classical precision limit, *Nature* **464**, 1165 (2010).
- [49] M. Kitagawa and M. Ueda, Squeezed spin states, *Phys. Rev. A* **47**, 5138 (1993).
- [50] M. Rigol, V. Dunjko, and M. Olshanii, Thermalization and its mechanism for generic isolated quantum systems, *Nature* **452**, 854 (2008).
- [51] R. Mondaini, K. R. Fratus, M. Srednicki, and M. Rigol, Eigenstate thermalization in the two-dimensional transverse field Ising model, *Phys. Rev. E* **93**, 032104 (2016).
- [52] R. Mondaini and A. Sur, Dataset for the paper "From Bell Products to GHZ: Quantum Memories via Emergent Hamiltonians," [10.5281/zenodo.17245519](https://zenodo.org/record/17245519) (2025).
- [53] E. V. H. Doggen, I. V. Gornyi, A. D. Mirlin, and D. G. Polyakov, Slow many-body delocalization beyond one dimension, *Phys. Rev. Lett.* **125**, 155701 (2020).
- [54] T.-M. Li, Z.-H. Sun, Y.-H. Shi, Z.-T. Bao, Y.-Y. Wang, J.-C. Zhang, Y. Liu, C.-L. Deng, Y.-H. Yu, Z.-H. Liu, C.-T. Chen, L. Li, H. Li, H.-T. Liu, S.-Y. Zhou, Z.-Y. Peng, Y.-J. Liu, Z. Wang, Y.-S. Xu, K. Zhao, Y. He, D. Feng, J.-C. Song, C.-P. Fang, J. Deng, M. Xu, Y.-T. Chen, B. Zhou, G.-H. Liang, Z.-C. Xiang, G. Xue, D. Zheng, K. Huang, Z.-A. Wang, H. Yu, P. Sierant, K. Xu, and H. Fan, Many-body delocalization with a two-dimensional 70-qubit superconducting quantum simulator (2025), [arXiv:2507.16882 \[quant-ph\]](https://arxiv.org/abs/2507.16882).
- [55] J. C. Peacock and D. Sels, Many-body delocalization from embedded thermal inclusion, *Phys. Rev. B* **108**, L020201 (2023).
- [56] Z.-H. Sun, F. B. Trigueros, Q. Tang, and M. Heyl, Probing prethermal nonergodicity through measurement outcomes of monitored quantum dynamics, *Phys. Rev. B* **112**, L180306 (2025).
- [57] I. Peschel and V. Eisler, Reduced density matrices and entanglement entropy in free lattice models, *Journal of Physics A: Mathematical and Theoretical* **42**, 504003 (2009).
- [58] M. A. Nielsen and I. L. Chuang, *Quantum Computation and Quantum Information: 10th Anniversary Edition* (Cambridge University, 2010).
- [59] P. Krantz, M. Kjaergaard, F. Yan, T. P. Orlando, S. Gustavsson, and W. D. Oliver, A quantum engineer's guide to superconducting qubits, *Applied Physics Reviews* **6**, 021318 (2019).
- [60] N. Shammah, S. Ahmed, N. Lambert, S. De Liberato, and F. Nori, Open quantum systems with local and collective incoherent processes: Efficient numerical simulations using permutational invariance, *Phys. Rev. A* **98**, 063815 (2018).
- [61] S. L. Braunstein and C. M. Caves, Statistical distance and the geometry of quantum states, *Phys. Rev. Lett.* **72**, 3439 (1994).
- [62] P. Hyllus, W. Laskowski, R. Krischek, C. Schwemmer, W. Wieczorek, H. Weinfurter, L. Pezzè, and A. Smerzi, Fisher information and multiparticle entanglement, *Phys. Rev. A* **85**, 022321 (2012).
- [63] L. Pezzè, A. Smerzi, M. K. Oberthaler, R. Schmied, and P. Treutlein, Quantum metrology with nonclassical states of atomic ensembles, *Rev. Mod. Phys.* **90**, 035005 (2018).
- [64] A. S. Sørensen and K. Mølmer, Entanglement and extreme spin squeezing, *Phys. Rev. Lett.* **86**, 4431 (2001).
- [65] G. Tóth, Multipartite entanglement and high-precision metrology, *Phys. Rev. A* **85**, 022322 (2012).

Appendix A: Approximate Emergent Hamiltonians in the many-body setting for two-dimensional systems

In the main text, Sec. III B, we argued that tackling the many-body case in more than one dimension leads to an elusive compact form for the emergent Hamiltonian, owing to the impossibility of mapping the problem to large spins. As such, one needs to rely on a truncation of Eq. (1), as done in other Hamiltonians [28, 29], whose truncation order n introduces an error $\mathcal{O}(t^n)$. In what follows, we explicitly compute the functional form of these approximate emergent Hamiltonians in two-dimensional lattices, focusing both on the case where one has only nearest-neighbor (NN) hoppings as well as when a homogeneous next-nearest-neighbor (NNN) hopping is included.

1. Two-dimensional nearest-neighbor approximate emergent Hamiltonian—Many excitations

Our starting point is the entangling Hamiltonian \hat{H}_f and the initial Hamiltonian \hat{H}_0 , given by

$$\hat{H}_f = \sum_{\mathbf{1}} \frac{\sqrt{l_x(L_x - l_x)}}{2} \left(\hat{a}_{\mathbf{1}+\hat{x}}^\dagger \hat{a}_{\mathbf{1}} + \text{H.c.} \right) + \sum_{\mathbf{1}} \frac{\sqrt{l_y(L_y - l_y)}}{2} \left(\hat{a}_{\mathbf{1}+\hat{y}}^\dagger \hat{a}_{\mathbf{1}} + \text{H.c.} \right), \quad \text{and} \quad (\text{A1})$$

$$\hat{H}_0 = \sum_{\mathbf{1}} (l_x + l_y) \hat{a}_{\mathbf{1}}^\dagger \hat{a}_{\mathbf{1}}. \quad (\text{A2})$$

Computing the truncated emergent Hamiltonian up to first order, which involves computing the commutator between \hat{H}_0 and \hat{H}_f , reads

$$\begin{aligned} \hat{\mathcal{M}}_{\text{NN}}^{(1)}(t) &= \hat{H}_0 - i t \hat{\mathcal{H}}_1 \\ &= \sum_{\mathbf{1}} (l_x + l_y) \hat{a}_{\mathbf{1}}^\dagger \hat{a}_{\mathbf{1}} - \frac{t}{2} \left[\sum_{\mathbf{1}} \sqrt{l_x(L_x - l_x)} \left\{ i \hat{a}_{\mathbf{1}}^\dagger \hat{a}_{\mathbf{1}+\hat{x}} + \text{H.c.} \right\} + \sum_{\mathbf{1}} \sqrt{l_y(L_y - l_y)} \left\{ i \hat{a}_{\mathbf{1}}^\dagger \hat{a}_{\mathbf{1}+\hat{y}} + \text{H.c.} \right\} \right]. \quad (\text{A3}) \end{aligned}$$

In the calculation of $\hat{\mathcal{H}}_1$, we make use of the hard-core boson commutation identities $[\hat{a}_{\mathbf{i}}, \hat{n}_{\mathbf{j}}] = \delta_{\mathbf{ij}} \hat{a}_{\mathbf{i}}$ and $[\hat{a}_{\mathbf{i}}^\dagger, \hat{n}_{\mathbf{j}}] = -\delta_{\mathbf{ij}} \hat{a}_{\mathbf{i}}^\dagger$, where $\hat{n}_{\mathbf{i}} = \hat{a}_{\mathbf{i}}^\dagger \hat{a}_{\mathbf{i}}$ is the number operator, which help evaluate commutators of the form $[\hat{a}_{\mathbf{i}}^\dagger \hat{a}_{\mathbf{j}}, \sum_{\mathbf{1}} w_{\mathbf{1}} \hat{n}_{\mathbf{1}}] = (w_{\mathbf{j}} - w_{\mathbf{i}}) \hat{a}_{\mathbf{i}}^\dagger \hat{a}_{\mathbf{j}}$. Given the nearest neighbor structure for the hopping terms in \hat{H}_f , this means that $w_{\mathbf{j}} - w_{\mathbf{i}} = w_{\mathbf{1}+\hat{x}} - w_{\mathbf{1}} = w_{\mathbf{1}+\hat{y}} - w_{\mathbf{1}} = 1$ for the \hat{H}_0 highlighted above. Finally, the physical interpretation of this first-order correction is to generate terms of current-like form, whose amplitude is modulated by the time t .

Proceeding to the second-order truncation, we compute

$$\begin{aligned} \hat{\mathcal{M}}_{\text{NN}}^{(2)}(t) &= \hat{H}_0 - i t \hat{\mathcal{H}}_1 - \frac{t^2}{2} \hat{\mathcal{H}}_2 \\ &= \sum_{\mathbf{1}} (l_x + l_y) \hat{a}_{\mathbf{1}}^\dagger \hat{a}_{\mathbf{1}} - \frac{t}{2} \left[\sum_{\mathbf{1}} \sqrt{l_x(L_x - l_x)} \left\{ i \hat{a}_{\mathbf{1}}^\dagger \hat{a}_{\mathbf{1}+\hat{x}} + \text{H.c.} \right\} + \sum_{\mathbf{1}} \sqrt{l_y(L_y - l_y)} \left\{ i \hat{a}_{\mathbf{1}}^\dagger \hat{a}_{\mathbf{1}+\hat{y}} + \text{H.c.} \right\} \right] \\ &\quad - \frac{t^2}{4} \left(\sum_{\mathbf{1}} (l_x - 1)(L_x - l_x + 1) \hat{a}_{\mathbf{1}}^\dagger \hat{a}_{\mathbf{1}} - \sum_{\mathbf{1}} l_x (L_x - l_x) \hat{a}_{\mathbf{1}}^\dagger \hat{a}_{\mathbf{1}} + \sum_{\mathbf{1}} (2l_x - L_x - 1) \hat{a}_{\mathbf{1}}^\dagger \hat{a}_{\mathbf{1}} \right. \\ &\quad \left. + \sum_{\mathbf{1}} (l_y - 1)(L_y - l_y + 1) \hat{a}_{\mathbf{1}}^\dagger \hat{a}_{\mathbf{1}} - \sum_{\mathbf{1}} l_y (L_y - l_y) \hat{a}_{\mathbf{1}}^\dagger \hat{a}_{\mathbf{1}} + \sum_{\mathbf{1}} (2l_y - L_y - 1) \hat{a}_{\mathbf{1}}^\dagger \hat{a}_{\mathbf{1}} \right. \\ &\quad \left. + 2 \sum_{\mathbf{1}} \sqrt{l_x(L_x - l_x)} \sqrt{l_y(L_y - l_y)} \left\{ \hat{a}_{\mathbf{1}+\hat{x}+\hat{y}}^\dagger \hat{a}_{\mathbf{1}+\hat{x}+\hat{y}} \hat{a}_{\mathbf{1}+\hat{x}}^\dagger \hat{a}_{\mathbf{1}+\hat{y}} - \hat{a}_{\mathbf{1}}^\dagger \hat{a}_{\mathbf{1}} \hat{a}_{\mathbf{1}+\hat{x}}^\dagger \hat{a}_{\mathbf{1}+\hat{y}} \right\} \right. \\ &\quad \left. + 2 \sum_{\mathbf{1}} \sqrt{l_x(L_x - l_x)} \sqrt{l_y(L_y - l_y)} \left\{ \hat{a}_{\mathbf{1}+\hat{x}+\hat{y}}^\dagger \hat{a}_{\mathbf{1}+\hat{x}+\hat{y}} \hat{a}_{\mathbf{1}+\hat{y}}^\dagger \hat{a}_{\mathbf{1}+\hat{x}} - \hat{a}_{\mathbf{1}}^\dagger \hat{a}_{\mathbf{1}} \hat{a}_{\mathbf{1}+\hat{y}}^\dagger \hat{a}_{\mathbf{1}+\hat{x}} \right\} \right), \quad (\text{A4}) \end{aligned}$$

where the second-order correction, proportional to t^2 , results in two types of terms: (1) renormalizations of the on-site energies already present in \hat{H}_0 , and (2), four-operator terms, with some compactly written as $\hat{n}_{\mathbf{l}'} \hat{a}_{\mathbf{1}+\hat{x}}^\dagger \hat{a}_{\mathbf{1}+\hat{y}}$, where $\mathbf{l}' = \hat{\mathbf{1}}$ or $\mathbf{1} + \hat{x} + \hat{y}$, that is, a density-assisted hopping term. In these calculations, we repeatedly employ the fundamental commutator identities for hard-core bosons:

$$[\hat{a}_{\mathbf{i}}^\dagger \hat{a}_{\mathbf{j}}, \hat{a}_{\mathbf{k}}^\dagger \hat{a}_{\mathbf{l}}] = \delta_{\mathbf{jk}} \hat{a}_{\mathbf{i}}^\dagger (1 - 2\hat{n}_{\mathbf{j}}) \hat{a}_{\mathbf{l}} - \delta_{\mathbf{il}} \hat{a}_{\mathbf{k}}^\dagger (1 - 2\hat{n}_{\mathbf{i}}) \hat{a}_{\mathbf{j}}, \quad (\text{A5})$$

$$[\hat{a}_{\mathbf{i}}^\dagger \hat{a}_{\mathbf{j}}, \hat{n}_{\mathbf{k}}] = (\delta_{\mathbf{jk}} - \delta_{\mathbf{ik}}) \hat{a}_{\mathbf{i}}^\dagger \hat{a}_{\mathbf{j}}. \quad (\text{A6})$$

These are the building blocks for simplifying the nested commutators appearing in $\hat{\mathcal{H}}_2$ into the diagonal and density-assisted hopping contributions written above.

2. Two-dimensional next-nearest neighbor—Many excitations

Similar calculations can be carried out in the case where one considers an extra next-nearest neighbor hopping term, here treated as homogeneous as in Eq. (13). The entangling and initial Hamiltonians read:

$$\begin{aligned} \hat{H}_f = & \sum_{\mathbf{1}} \frac{\sqrt{l_x(L_x - l_x)}}{2} \left(\hat{a}_{\mathbf{1}+\hat{x}}^\dagger \hat{a}_{\mathbf{1}} + \text{H.c.} \right) + \sum_{\mathbf{1}} \frac{\sqrt{l_y(L_y - l_y)}}{2} \left(\hat{a}_{\mathbf{1}+\hat{y}}^\dagger \hat{a}_{\mathbf{1}} + \text{H.c.} \right) \\ & + J_\times \sum_{\mathbf{1}} \left[\left(\hat{a}_{\mathbf{1}+\hat{y}-\hat{x}}^\dagger \hat{a}_{\mathbf{1}} + \text{H.c.} \right) + \left(\hat{a}_{\mathbf{1}+\hat{y}+\hat{x}}^\dagger \hat{a}_{\mathbf{1}} + \text{H.c.} \right) \right], \end{aligned} \quad (\text{A7})$$

$$\hat{H}_0 = \sum_{\mathbf{1}} (l_x + l_y) \hat{a}_{\mathbf{1}}^\dagger \hat{a}_{\mathbf{1}}. \quad (\text{A8})$$

In this case, up to the first order in the truncation, the emergent Hamiltonian results in

$$\begin{aligned} \hat{\mathcal{M}}_{\text{NNN}}^{(1)}(t) &= \hat{H}_0 - it \hat{\mathcal{H}}_1 \\ &= \hat{\mathcal{M}}_{\text{NN}}^{(1)}(t) + \left\{ (-it) J_\times \left[\sum_{\mathbf{1}} \hat{a}_{\mathbf{1}-\hat{x}+\hat{y}}^\dagger \hat{a}_{\mathbf{1}} - \sum_{\mathbf{1}} \hat{a}_{\mathbf{1}+\hat{x}+\hat{y}}^\dagger \hat{a}_{\mathbf{1}} \right] + \text{H.c.} \right\}, \end{aligned} \quad (\text{A9})$$

where $\hat{\mathcal{M}}_{\text{NN}}^{(1)}(t)$ is defined in Eq. (A3). This shows that the extra hopping terms lead to current-like terms among the next-nearest neighbor sites.

Appendix B: THE EFFECTS OF ENVIRONMENTAL NOISE

The Emergent Hamiltonian protocol described in Secs. II–V is exact at the level of unitary dynamics: if the system is evolved under an entangling Hamiltonian \hat{H}_f up to a time t_{freeze} and then quenched to the corresponding emergent Hamiltonian $\hat{\mathcal{M}}(t_{\text{freeze}})$ [Eq. (1) and its closed forms such as Eqs. (5), (10) and (20)], the many-body state $|\psi(t_{\text{freeze}})\rangle$ is stationary (up to a global phase) because it is an eigenstate of $\hat{\mathcal{M}}(t_{\text{freeze}})$. Actual devices, however, are never perfectly isolated, and the stored state will ultimately degrade due to coupling to uncontrolled environmental degrees of freedom. In this section we quantify how such noise limits the lifetime of the memory, in particular for the GHZ state discussed in Sec. V.

We include Markovian energy relaxation and dephasing during the post-quench memory (storage) stage. The preparation dynamics under \hat{H}_{OAT} is taken to be unitary. Noise is incorporated in the storage stage through coherence times T_1 and T_2 : relaxation is implemented with rate $1/T_1$, while dephasing is included so as to reproduce the prescribed transverse coherence time T_2 , consistent with the standard decoherence model for superconducting qubits [59].

All simulations are performed in the natural units of the OAT Hamiltonian $H = -\lambda S_z^2$ with $\hbar = 1$, using dimensionless time $t = \lambda_{\text{phys}} t_{\text{phys}}$. To connect with superconducting-circuit implementations, we consider an interaction strength $\lambda_{\text{phys}}/(2\pi) \approx 2$ MHz, corresponding to $\lambda_{\text{phys}} = 4\pi \times 10^6$ s⁻¹, and adopt representative coherence times $T_1^{\text{phys}} = 34$ μs and $T_2^{\text{phys}} = 20$ μs [45]. Expressed in natural units via

$$T_\alpha = \lambda_{\text{phys}} T_\alpha^{\text{phys}},$$

this yields the dimensionless decay times $T_1 \approx 136\pi \approx 4.3 \times 10^2$ and $T_2 \approx 80\pi \approx 2.5 \times 10^2$, which are used throughout the analysis. The noisy dynamics are simulated using the permutationally invariant quantum solver (PIQS), which exploits collective symmetry to efficiently evolve the system within the Dicke manifold [60].

Figure 8 characterizes the stability of the stored GHZ state under relaxation and dephasing. We denote by $\rho(t)$ the many-body density matrix of the system at time t , obtained from the Lindblad evolution. As in Sec. V, we work in the rotated frame defined by $\hat{R}_x(-\pi/2) = e^{+i(\pi/2)\hat{S}_x}$ and $\tilde{\rho}(t) = \hat{R}_x(+\pi/2)\rho(t)\hat{R}_x(-\pi/2)$, so that the equatorial GHZ produced by the OAT dynamics is mapped to the computational GHZ state within subspace spanned by $\{|0 \cdots 0\rangle, |1 \cdots 1\rangle\}$.

The memory performance is first quantified by the GHZ fidelity in Fig. 8(a)

$$F(t) = \text{Tr}[|\text{GHZ}_\phi\rangle \langle \text{GHZ}_\phi| \tilde{\rho}(t)] = \langle \text{GHZ}_\phi | \tilde{\rho}(t) | \text{GHZ}_\phi \rangle, \quad |\text{GHZ}_\phi\rangle = \frac{|0 \cdots 0\rangle + e^{i\phi} |1 \cdots 1\rangle}{\sqrt{2}},$$

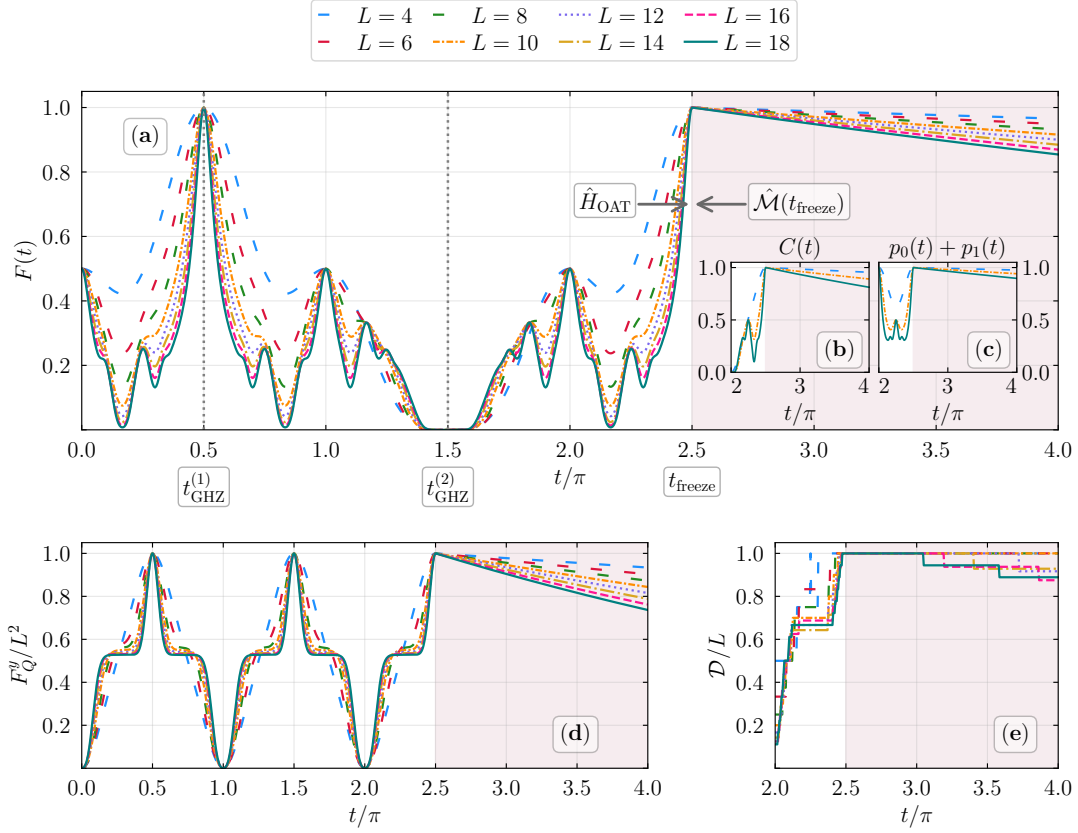


FIG. 8. Impact of Markovian relaxation and dephasing on the GHZ-memory protocol of Sec. V; we use values of T_1 and T_2 typical to experiments [45]. A GHZ state is generated under $\hat{H}_{\text{OAT}} = -\lambda \hat{S}_z^2$ and then frozen by quenching to $\hat{\mathcal{M}}(t_{\text{freeze}})$ at $t_{\text{freeze}} = t_{\text{GHZ}}^{(1)} + 2\pi$. Noise acts only during the post-quench storage stage. (a) GHZ fidelity $F(t)$. (b) GHZ coherence $C(t)$. (c) Sum of populations $p_0(t)$ and $p_1(t)$ of $|0 \cdots 0\rangle$ and $|1 \cdots 1\rangle$. (d) Quantum Fisher information $\mathcal{F}_Q^{(y)}(t)/L^2$ with respect to \hat{S}_y . (e) Entanglement depth $\mathcal{D}(t)/L$ inferred from QFI-based k -producibility bounds. See text for definitions of $F(t)$, $C(t)$, $p_{0,1}(t)$, $\mathcal{F}_Q^{(y)}$, and the QFI-based entanglement depth $\mathcal{D}(t)$.

with the phase ϕ fixed by the unitary evolution at $t = t_{\text{GHZ}}^{(1)}$. To separate coherence loss from population leakage, we monitor the edge populations

$$p_0(t) = \langle 0 \cdots 0 | \tilde{\rho}(t) | 0 \cdots 0 \rangle, \quad p_1(t) = \langle 1 \cdots 1 | \tilde{\rho}(t) | 1 \cdots 1 \rangle,$$

and the off-diagonal coherence between these two components in Fig. 8(b)

$$C(t) = 2 |\langle 0 \cdots 0 | \tilde{\rho}(t) | 1 \cdots 1 \rangle|.$$

In Fig. 8(c), we examine $p_0(t) + p_1(t)$ to quantify the population remaining in the GHZ manifold.

To assess metrological usefulness, we compute the quantum Fisher information [61]

$$\mathcal{F}_Q[\rho(t), \hat{A}] = 2 \sum_{k,\ell} \frac{(\lambda_k - \lambda_\ell)^2}{\lambda_k + \lambda_\ell} \left| \langle k | \hat{A} | \ell \rangle \right|^2,$$

with $\rho(t) = \sum_k \lambda_k |k\rangle \langle k|$ and $\hat{A} = \hat{S}_y$. In Fig. 8(d) we plot $\mathcal{F}_Q^{(y)}(t)/L^2$, so that an ideal GHZ corresponds to a value of order unity, reflecting Heisenberg scaling $\mathcal{F}_Q \sim L^2$ [62, 63].

Finally, we quantify genuine multipartite entanglement through the entanglement depth \mathcal{D} . By definition, \mathcal{D} [64] is the size of the largest subset of qubits that must be genuinely entangled with each other: $\mathcal{D} = 1$ corresponds to fully separable states, while $\mathcal{D} = L$ implies that all L qubits share genuine multipartite entanglement. Entanglement depth captures globally shared entanglement in contrast to merely pairwise entanglement, making it particularly meaningful for states such as GHZ, whose defining feature is macroscopic, system-wide entanglement.

Operationally, we infer a "minimum" depth from the maximal QFI over collective directions, $\mathcal{F}_Q^{\max}(t) = \max\{\mathcal{F}_Q[\rho(t), \hat{S}_x], \mathcal{F}_Q[\rho(t), \hat{S}_y], \mathcal{F}_Q[\rho(t), \hat{S}_z]\}$. For an L qubit k -producible state one has the bound $\mathcal{F}_Q^{\max} \leq sk^2 + r^2$, with $s = \lfloor L/k \rfloor$ and $r = L - sk$ [62, 65]. A violation of this inequality certifies that the entanglement depth is at least $k + 1$. The resulting $\mathcal{D}(t)$, normalized by L , is shown in Fig. 8(e).

Several trends are apparent. The GHZ fidelity in Fig. 8(a) remains comparatively robust over the simulated storage window. The QFI in Fig. 8(d) decays faster than the fidelity, reflecting its stronger sensitivity to small losses of coherence, yet it remains sizable for a substantial fraction of the post-quench evolution. Figures 8(b) and 8(c) show that the coherence $C(t)$ decreases more rapidly than the total GHZ weight $p_0(t) + p_1(t)$, consistent with dephasing suppressing the off-diagonal element between the two macroscopic branches before significant population leakage occurs. Finally in Fig. 8(e), the entanglement depth remains maximal, $\mathcal{D}(t) = L$, over the simulated times for smaller system sizes, while a reduction of the certified depth becomes visible only for larger systems (here starting at $L = 12$), reflecting the increased sensitivity of larger GHZ states to decoherence. Overall, for representative superconducting coherence times, the emergent-Hamiltonian protocol maintains a fairly high fidelity with the target GHZ state over the simulated durations. While metrological gain degrades earlier than fidelity, the QFI-based witness continues to certify large, and often maximal, multipartite entanglement depth over a substantial portion of the storage window.